Detailed dynamic Solid Oxide Fuel Cell modeling for electrochemical impedance spectra simulation

Ph. Hofmann[a], K.D. Panopoulos[b],*

[a] Laboratory of Steam Boilers and Thermal Plants, School of Mechanical Engineering, Thermal Engineering Section, National Technical University of Athens, Heroon Polytechniou 9, 15780 Athens, Greece
[b] Institute for Solid Fuels Technology and Applications, Centre for Research and Technology Hellas, 4th km. Ptolemais-Mpodosakeio Hospital, Region of Kouri, P.O. Box 95, GR 502, 50200 Ptolemais, Greece

ARTICLE INFO

ABSTRACT

This paper presents a detailed flexible mathematical model for planar solid oxide fuel cells (SOFCs), which allows the simulation of steady-state performance characteristics, i.e. voltage–current density (V–j) curves, and dynamic operation behavior, with a special capability of simulating electrochemical impedance spectroscopy (EIS). The model is based on physico-chemical governing equations coupled with a detailed multi-component gas diffusion mechanism (Dusty-Gas Model (DGM)) and a multi-step heterogeneous reaction mechanism implicitly accounting for the water-gas-shift (WGS), methane reforming and Boudouard reactions. Spatial discretization can be applied for 1D (button-cell approximation) up to quasi-3D (full size anode supported cell in cross-flow configuration) geometries and is resolved with the finite difference method (FDM). The model is built and implemented on the commercially available modeling and simulations platform gPROMS™. Different fuels based on hydrogen, methane and syngas with inert diluents are run. The model is applied to demonstrate a detailed analysis of the SOFC inherent losses and their attribution to the EIS. This is achieved by means of a step-by-step analysis of the involved transient processes such as gas conversion in the main gas chambers/channels, gas diffusion through the porous electrodes together with the heterogeneous reactions on the nickel catalyst, and the double-layer current within the electrochemical reaction zone. The model is an important tool for analyzing SOFC performance fundamentals as well as for design and optimization of materials' and operational parameters.

1. Introduction

1.1. The solid oxide fuel cell

An operating solid oxide fuel cell (Fig. 1) produces electrical power by converting part of the chemical energy of a fuel while the rest is rejected as heat due to the oxidation reactions. The global hydrogen oxidation reaction, which is assumedly the fastest electrochemical reaction within an SOFC is:

$$H_2 + \frac{1}{2}O_2 \Leftrightarrow H_2O \tag{1}$$

The electrical potential reaches its theoretical maximum E_{rev} (=reversible potential) at electrochemical equilibrium, i.e. zero current operation (unpolarized cell or open circuit voltage – OCV) and chemical equilibrium of reactants and products. This is related to the Gibbs free energy of the electrochemical reaction through the following equation:

$$E_{rev} = -\frac{\Delta G}{nF} = -\frac{\Delta G^\circ}{nF} - \frac{RT}{nF}\ln Q \tag{2}$$

The first part of the right hand side equation is the temperature-dependent standard potential E° and the second part describes the influence of reactants' activities (here partial pressures) expressed through the reaction quotient Q of the electrochemical reaction. Substituting the reaction quotient Q with partial pressure terms and the first part of the right hand side equation with the temperature-dependent standard potential E°, Eq. (2) results in the well-known

Nomenclature

$a_{O^{2-}}$	activity of bulk oxygen ions (Kroeger–Vink notation)
a_{Ni}	specific surface area of Nickel catalyst ($cm^2\,cm^{-3}$)
$a_{V_O^{\bullet\bullet}}$	activity of electrolyte bulk vacancies (Kroeger–Vink notation)
A	area (m^2)
A_{cell}	solid oxide fuel cell active area (m^2)
A_{ch}	gas channel cross-section area (m^2)
A_i	pre-exponential factor of reaction i (units vary) (mol, cm, s)
$c_{el,k}$	gas phase species concentration ($mol\,cm^{-3}$) or surface species concentration ($mol\,cm^{-2}$)
C	electrical double-layer capacitance ($F\,cm^{-2}$)
d_{an}	anode thickness (m)
d_{ca}	cathode thickness (m)
$d_{electrolyte}$	electrolyte thickness (m)
$D_{k,j}$	binary diffusion coefficient ($cm^2\,s^{-1}$)
$D_{KN,k}$	Knudsen diffusion coefficient ($cm^2\,s^{-1}$)
E	voltage (V)
$E_{a,i}$	activation energy of reaction i ($J\,mol^{-1}\,K^{-1}$)
E_{cell}	electrical potential of the SOFC (V)
E°	standard potential (temperature-dependent) (V)
E_i	activation energy for electrolyte conductivity ($J\,mol^{-1}\,K^{-1}$)
E_p	amplitude of alternating cell voltage output (V)
f	frequency (Hz)
F	Faraday constant $= 6.023 \times 10^{23} \times 1.602 \times 10^{-19}$ ($Cb\,mol^{-1}$)
ΔG	molar Gibbs free energy change of reaction (1) ($J\,mol^{-1}$)
ΔG°	standard molar Gibbs free energy change of reaction (1) ($J\,mol^{-1}$)
h	height (m)
I	current (A)
I_{all}	number of irreversible elementary reactions
I_{ad}	number of adsorption reactions
I_{gain}	gain current amplitude for EIS (A)
j	current density ($A\,cm^{-2}$)
$j_{0,el}$	exchange current density ($A\,cm^{-2}$)
J_{bias}	bias current density for EIS ($A\,cm^{-2}$)
$j_{F,el}$	Faradaic current density ($A\,cm^{-2}$)
K_{an}	number of chemical species at the anode side
$K_{g,an}$	number of gaseous chemical species at the anode side
K_s	number of surface chemical species at the anode side
l	cell length (m)
$\dot{m}_{ch}$	mass flow ($kg\,s^{-1}$)
MW_k	molecular weight of species k
n	number of electrons transferred in reaction (1)
$\dot{n}_k$	molar flux of species k ($mol\,s^{-1}\,cm^{-2}$)
$\dot{N}$	volume flow ($L\,s^{-1}$)
p_i	partial pressure of component i (atm)
$P_{el,tot}$	total pressure of electrode channel (bar)
P_{op}	the SOFC operating pressure (bar)
Q	reaction quotient
$\dot{r}_i$	adsorption reaction rates ($mol\,cm^{-2}\,s^{-1}$)
r_{pore}	pore diameter (m)
$\dot{r}_{TPB}$	electrochemical reaction rate ($mol\,cm^{-2}\,s^{-1}$)
R	area-specific resistance ($Ohm\,cm^2$)
R_g	ideal gas constant ($8.314\,J\,mol^{-1}\,K^{-1}$)
R_{ohm}	ohmic electric area-specific resistance ($ohm\,cm^2$)

$\dot{s}_k$	Species net molar production rate ($mol\,cm^{-2}\,s^{-1}$)
t	time (s)
T	temperature (K)
u_{ch}	gas velocity in channels ($m\,s^{-1}$)
w	width (m)
W_{ch}	width of channel plus part under interconnect rib (m)
U_f	fuel utilization factor ($-$)
U_o	oxygen utilization factor ($-$)
V	voltage (V)
V_{ch}	gas channel/chamber volume (m^3)
V_m^0	standard molar volume ($mol\,L^{-1}$)
x	dimension x
X	mole fraction ($-$)
y	dimension x
Y	mass fraction ($-$)
z	dimension z
Z	impedance ($Ohm\,cm^2$)

Greek letters

$\alpha_{an,el}$	anodic symmetry factor for Butler–Volmer equation ($-$)
$\alpha_{ca,el}$	cathodic symmetry factor for Butler–Volmer equation ($-$)
β_i	temperature exponent ($-$)
γ_i	sticking coefficient ($-$)
Γ	available surface site density ($mol\,cm^{-2}$)
ε	porosity ($-$)
ε_i	surface site fraction-dependent activation energy ($-$)
$\eta_{ohm,act,conc}$	overpotentials due to ohmic, activation, concentration losses (V)
θ	surface site fraction ($-$)
ν	period (s^{-1})
ν_{ki}	the difference between stoichiometric coefficients of products and reactants of the kth species in the ith reaction.
ρ_{ch}	gas density in channel ($kg\,m^{-3}$)
σ_i	electrolyte conductivity ($S\,cm^{-1}$)
σ_0	parameter for electrolyte conductivity ($S\,K^{-1}\,cm^{-1}$)
τ	tortuosity ($-$)
φ	phase angle ($^{\circ}$)
$\Phi_{e,el}$	electrode (anode or cathode) electronic potential (V)
$\Phi_{i,el}$	electrode (anode or cathode) ionic potential (V)
$\Delta\Phi_{el}$	potential step in electrode (anode or cathode) (V)

Subscripts

an	anode
bias	biased variable
ca	cathode
cell	total cell
ch	channel (i.e. anode or cathode side)
e	electronic
el	electrode: el = an for anode and el = ca for cathode
eq	equilibrium
dl	double layer
F	Faradaic
i	ionic phase (when used in Φ)
i	reaction counter
in	input
k	species counter
ohm	ohmic

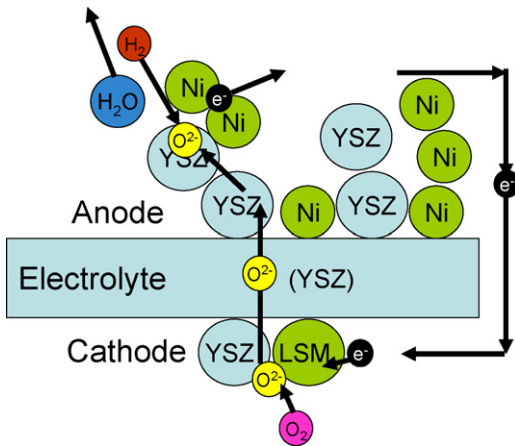|	
p	peak (when used with f)
rev	reversible
tot	total

Superscript
in   input

Fig. 1. Schematic representation of an SOFC operating.

Nernst equation:

$$E_{rev} = E^{\circ} + \frac{RT}{2F} \ln \left(\frac{p_{H_2} p_{O_2}^{1/2}}{p_{H_2O}} \right) \qquad (3)$$

When the fuel cell is connected to a load through a closed circuit, a current is produced through the electrochemical reactions and the cell's potential is reduced by internal non-reversible voltage losses η which depend on the current and derive from the following three mechanisms:

- *Ohmic resistance losses* η_{ohm}: which occur in the solid electrolyte phases (e.g. YSZ or GDC) due to ions flow and in the electrode phases (Ni, LSM, etc.) and metallic interconnects due to electrons flow.
- *Concentration overpotentials* η_{conc}: reduced Nernst potential at the electrochemically active reaction zone (triple phase boundary – TPB) due to depletion of charge carrying reactants caused by slow diffusion from the bulk of the gas chambers/channels through the porous electrodes.
- *Activation overpotentials* η_{act}: reduced electrochemical potential because energy is needed to drive the electrochemical reactions in the desired forward direction, i.e. reduction of oxygen at the cathode and oxidation of hydrogen at the anode.

The operating cell potential thus can be expressed as a subtraction of the different losses from the reversible potential [1–4]:

$$E_{cell} = E_{rev} - \eta(j)$$
$$= E_{rev} - \eta_{ohm} - \eta_{conc,an} - \eta_{conc,ca} - \eta_{act,an} - |\eta_{act,ca}| \qquad (4)$$

According to Bessler [5], Eq. (4) gives indeed a good picture of the contribution from the different kinds of loss mechanisms, however these voltage losses do not represent physical meaningful potential steps. In reality, three different potential levels exist within the fuel cell system. These are the cathode electronic phase (electrode)

potential $\Phi_{e,ca}$, the ionic phase (electrolyte) potential Φ_i and the anode electronic phase (electrode) potential $\Phi_{e,an}$. The potential difference between cathode and anode constitutes the operating cell potential:

$$E_{cell} = \Phi_{e,ca} - \Phi_{e,an} \qquad (5)$$

It results from two potential steps occurring:

(1) at the cathode/electrolyte interface:

$$\Delta\Phi_{ca} = \Phi_{e,ca} - \Phi_{i,ca} \qquad (6)$$

(2) and at the anode/electrolyte interface:

$$\Delta\Phi_{an} = \Phi_{e,an} - \Phi_{i,an} \qquad (7)$$

Since the state-of-the art SOFC electrodes contain both electrode and electrolyte phases in form of distributed particles (e.g. Ni (electronic) and YSZ (ionic) in the anode), the potential steps vary within a certain depth of the porous anode and cathode electrodes. This potential distribution is confined to the electrochemical active reaction zone, the so-called triple phase boundary (TPB), where all reactants and products can meet and proceed with the electrochemical reactions: Ionic O^{2-} (in electrolyte phase), gas reactants in the electrode pores and electrons (in the electrode phases). The TPB is situated near the electrolyte membrane and electrode interface and extents typically a few ten microns [6] into the electrode depending on parameters such as the TPB length (active reaction zone), phase conductivities and gas phase activities.

The unpolarized cell is in electrochemical equilibrium, and the equilibrium potential steps given by Eqs. (9) and (11) arise from the reduction potentials of the respective half-cell electrochemical reactions Eqs. (8) and (10) [7]:

Cathode:

$$\frac{1}{2}O_2 + 2e^- \Leftrightarrow O^{2-} \qquad (8)$$

$$\Delta\Phi_{eq,ca} = E^{\circ}_{O_2/O^{2-}} - \frac{RT}{2F} \ln \left(\frac{a_{O^{2-}}}{p_{O_2}^{0.5} \cdot a_{V_O^{\bullet\bullet}}} \right) \qquad (9)$$

Anode:

$$H_2 + O^{2-} \Leftrightarrow H_2O + 2e^- \qquad (10)$$

$$\Delta\Phi_{eq,an} = E^{\circ}_{H_2O/H_2} - \frac{RT}{2F} \ln \left(\frac{p_{H_2} \cdot a_{O^{2-}}}{p_{H_2O} \cdot a_{V_O^{\bullet\bullet}}} \right) \qquad (11)$$

Their difference equals the reversible cell potential E_{rev} given by the Nernst Eq. (3) for the global reaction Eq. (1).

The drop in ionic phase potential Φ_i occurs mainly in the dense electrolyte membrane but also to a certain extent within the anodic and cathodic electrochemical reaction zones (TPB) where the oxygen ions migrate from and into the respective electrodes to take part in the distributed charge-transfer. The more the TPB extends into the electrode, the higher are the ionic ohmic losses because the oxygen ion needs to pass through the electrolyte particles which have typically much smaller conductivity than the bulk electrolyte membrane due to the porous and distributed nature of the electrolyte/electrode cermet. The drop in electrode potentials along the electrode thickness due to electrons transfer is negligible due to the high electronic conductivity, thus $\Phi_{e,ca}$ and $\Phi_{e,an}$ can be considered approximately constant.

The concentration overpotentials represent a difference between the larger potential step $\Delta\Phi_{an,b}$ at the electrode/gas chamber (or channel) interface and the smaller potential step $\Delta\Phi_{an,TPB}$ at the TPB. Their cause can be deducted from Fig. 2 and lies in the different half-cell reduction potentials $\Delta\Phi_{eq,el}$ due to diffusion induced reactants partial pressure gradients. Fig. 2 additionally
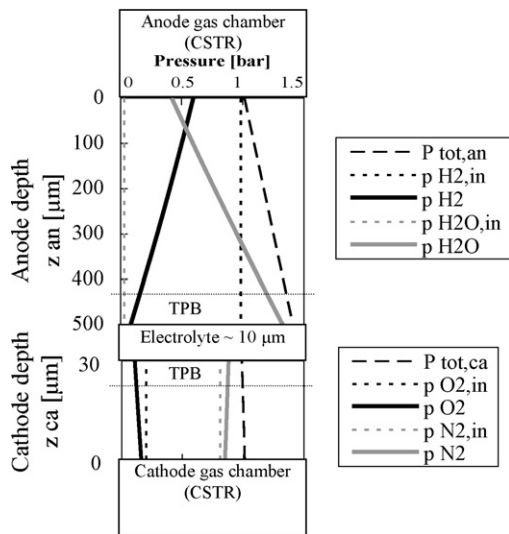
Fig. 2. Partial pressure distribution within the porous electrodes for the anodic H_2/H_2O and cathodic O_2/N_2 systems (1D).

shows that the electrode/gas chamber (or channel) interface partial pressures differ from the inlet partial pressures due to fuel and oxygen depletion (utilization) when the inlet flows are kept constant during polarization. This results in an additional reduction of the half-cell reduction potentials and is a material and geometry independent purely thermodynamic loss.

Activation overpotentials given by Eqs. (12) and (13) decrease the potential difference within the electrochemical reaction zone (TPB) due to the additional energy required to drive the electrochemical reactions into the desired forward reaction. These losses are in equilibrium with the ionic ohmic losses within the TPB: the higher the electrochemical reaction rates and/or the larger the available TPB, the less do the oxygen ions need to travel into the electrodes and vice versa.

$$\eta_{act,ca} = \Delta\Phi_{ca} - \Delta\Phi_{eq,ca} \qquad \text{where } \Delta\Phi_{ca} < \Delta\Phi_{eq,ca} \qquad (12)$$

$$\eta_{act,an} = \Delta\Phi_{an} - \Delta\Phi_{eq,an} \qquad \text{where } \Delta\Phi_{an} < \Delta\Phi_{eq,an} \qquad (13)$$

The above described origin of the cell potential E_{cell} resulting from the three different potential levels within the fuel cell includes implicitly the different losses given in Eq. (4) which reduce the two half-cell reduction potentials.

1.2. Electrochemical impedance spectroscopy

Electrochemical impedance spectroscopy is a widely used tool for solid oxide fuel cell (SOFC) performance and materials analysis [3,8–10]. The common approach of fitting the impedance spectra with equivalent electrical circuit models is good enough for overall performance comparison, but lacks accuracy in explaining the physical source of the different losses, especially due to the usually overlapping arcs of the spectrum.

In theory, each transport process occurring in the SOFC should have its own arc in the electrochemical impedance spectrum (EIS). Due to their capacitive nature, the transport processes need a certain time to relax when perturbed by a changing boundary condition. In practical SOFC impedance measurements, this is typically a sinusoidal AC current or voltage on top of a DC bias which is varied for a range of frequencies in order to generate the EIS. The capacitances for the main transport processes are mass (function of reactor volume and mass density) for mass transport, heat capacity for heat transport and double-layer capacitance for charge transport between ionic and electronic conductive phases.

In SOFC impedance measurements, the dependent output signal (in this work the voltage) has the same frequency as the perturbing input signal (here the current) but due to the capacitances is shifted by a negative phase angle and thus manifests itself as arcs on the negative imaginary impedance axis. The width of these arcs on the real axis express the relaxation time distributions of the respective transport processes and are related to their resistances: the transport process are inhibited by convective and diffusive velocities, chemical kinetics, heat conductivity and charge-transfer kinetics, respectively. These arcs have the shape of a semi-circle (or similar) and they express the range of frequencies for which the particular transport process is sensitive. The peak frequency is the inverse of the characteristic relaxation time of the underlying transport process.

In practice, the electrochemical impedance spectrum (simulated or measured) manifests itself as a superimposition of arcs of different sizes originating from the underlying transport processes. Thus the different overpotential contributions cannot clearly be distinguished. When the transient term of a transport process equation ($\partial/\partial t = 0$) is set to zero, the equation's output values immediately adapt to the varying input signal. This simulated periodic stationary behavior with no capacitive inertia results in no signal on the imaginary axis of the EIS. The real axis however is not affected and thus the relevant process resistances are still effective. In this work, this is taken advantage of in order to break down the EIS into the different main contributing loss mechanisms.

EIS is a rather sensitive measurement method. Only a linear (or pseudo-linear) system results in a sinusoidal phase-shifted response at the same frequency as the sinusoidal perturbation signal [11]. The cell's response is pseudo-linear when the amplitude of the input signal is small and measurements are done in pseudo-linear part of the V–j-curve. In the highly non-linear part of the V–j-curve, EIS spectra can loose their linear behavior. Another common cause of problems in EIS measurements and their analysis is a drift in the system being measured due to non-stationary initial state. External factors such as wiring of the current and voltage measurement leads can cause additional capacitive or inductive impedance features in EIS measurements often observed as high and/or low frequency artifacts [10,12]. A detailed analysis of experimental errors in EIS measurement is given by Cimenti et al. [13,14].

2. Mathematical model description

The development of a distributed model of single planar SOFCs was started on the EES^{TM} simultaneous equation solver platform where a quasi-2D steady-state model was implemented as presented by the authors in [15], in which spatial distribution in the membrane plane (x- and y-direction) were solved via the Finite Volume Method (FVM). In the current work, a more complex dynamic SOFC model capable of simulating 1D, 2D and quasi-3D geometries was built in gPROMS^{TM}. The potential step approach presented in Section 1, a detailed porous electrode gas diffusion mechanism, detailed anode and cathode activation overpotential description and EIS simulation routines were included. Fig. 3 shows that the 2D and quasi-3D models are spatial extensions of the 1D case which only considers the distributed electrodes (z-direction) and is a good approximation of so-called button-cell experimental set-ups. For the 2D models, the equations of both the anodic and the cathodic systems are additionally distributed in the x-direction representing parallel fuel and oxidizer (air) channels. Depending on the boundary conditions and discretization methods, both co- and counter-flow configurations can be simulated. The quasi-3D model includes electrodes discretization in the z-direction, fuel channel discretization in the x-direction and oxidizer channel discretization in the y-direction resulting in a cross-flow configuration where
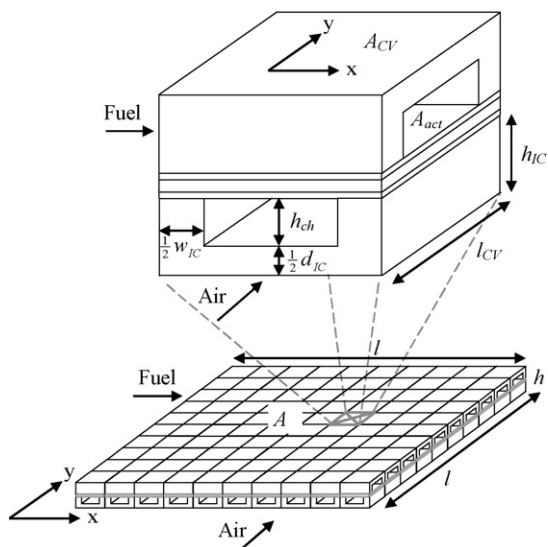
Fig. 3. A quasi-3D SOFC in cross-flow configuration where each control volume or node point in the x–y plane produces 1D results as in Fig. 2.

the channels are perpendicular to each other. With both the 2D and quasi-3D models, full size SOFCs with their spatial variation of variables can be simulated. Spatial discretization is resolved with the finite difference method (FDM).

The following main assumptions and simplifications are the basis of the model:

- H_2 is considered as the only electrochemical active compound (due to its fast reaction kinetics) and thus the Nernst potential and activation losses only depend on the H_2 oxidation reaction Eq. (1).
- For 1D: The gas chambers above the porous electrodes are modeled as perfectly stirred reactors (PSTR) with no gas stagnation layer. For further readings on gas stagnation layer effects see [16–18,4].
- For 2D and quasi-3D: The gas flow in the anode and cathode gas channels is modeled as plug flow neglecting boundary layer flow and axial diffusion. For axial diffusion effects see [19,20].
- Hydro-dynamics were neglected, thus no pressure loss in gas chambers/channels is considered.
- The D'Arcy viscous flux term (pressure driven flux) of the Dusty-Gas Model (DGM) for the porous electrodes was neglected since it does not have any significant effect on performance results. Transport limitations are in the diffusion-controlled regime due to the small pore sizes [21,22].
- Equi-potential current collection is a common assumption due to the negligible electronic ohmic losses within the electrodes.
- Activation overpotentials due to charge-transfer kinetics is modelled with a modified Butler–Volmer type approach and no distributed charge-transfer is considered (H_2 oxidation occurs at the Triple Phase Boundary (TPB) which is reduced to the electrode/electrolyte membrane interface). This approach is considered by Zhu and Kee [23] to be accurate enough, especially for anode supported cells (ASC) in comparison with the more complex distributed charge-transfer and additional elementary electrochemical kinetics approach.
- Mean field approximation: No distribution of microstructural parameters such as pore size, particle size and tortuosity in electrodes is considered.
- Isothermal operation is modelled which is a good approximation for single button and full size cell experiments. For modelling of SOFC stacks, temperature distributions occur and a thermal model needs to be appended as in [15].

The following subsections give a detailed presentation of all necessary equations of the model which can be bundled into several main groups: mass transport equations in gas chambers/channels and in the porous electrodes, a detailed multi-component porous media diffusion mechanism for the electrodes, a heterogeneous catalytic reforming mechanisms (HCR) of elementary gas-surface and surface reactions, detailed potential step approach, Butler–Volmer type activation overpotentials and the EIS simulation.

Domains, boundary conditions (for the transport equations containing partial spatial derivatives) and initial conditions (for the transient equations) are given in the respective equations tables as well as the species (k) and reaction (i) counter variables. Domains are either open, denoted by brackets (), closed [], or a combination of both. The boundary conditions (B.C.) are additional equations to close the domains. Initial conditions (I.C.) are valid within the domains of the respective equations.

Standard equations converting between the different forms of concentration and partial pressures (molar fraction X, mass fraction Y, molar concentration c, density ρ, partial pressure p_i) are not presented for the sake of brevity. Also the unit conversion factors, e.g. between kmol and mol and min and s, etc. are left out in order to make the equations more readable.

For V–j-curve simulation, the transient parts of the equations are set to zero to obtain steady-state equations. Everything else is modelled with the same equations so that it is not necessary to present the steady-state performance model explicitly. Alternatively the V–j-curves can be simulated with the dynamic model awaiting steady-state for each current set-point.

2.1.1. Mass transport

2.1.1.1. Transport equations

The model's governing mass transport equations are given in Table 1. Button-cell experimental set-ups can be very well approximated by a 1D model where the gas chambers above the electrodes are modeled as perfectly stirred reactors (PSTR) with a uniform bulk gas composition, given by Eq. (14).

For 2D and quasi-3D models, the species conservation in the gas channels is evaluated as plug flow by Eq. (15) together with Eq. (16) to obtain total mass conservation. For 2D co- and counter-flow, the equations and variables are both distributed in x-direction. Since the anode and cathode channels are parallel, it is sufficient to calculate one channel with correspondingly reduced anode and cathode inlet flows in order to obtain the same results as for a full sized cell.

For all models, the porous media transport equations (distribution in z-direction) are considered purely diffusive as given by Eq. (17) together with Eq. (18) for the total mass balance. The species molar fluxes $\dot{n}_k$ are evaluated by the Dusty-Gas Model (DGM) through an implicit relationship with the concentration gradients within the porous electrodes described in Eq. (21), and depend on the boundary conditions at the electrode/electrolyte membrane interface. These connect the mass transport model to the electrochemistry through Faraday's law Eq. (35). The mass sources/sinks are the species net molar production rates from the HCR given by Eq. (25) and are only applicable for methane/syngas fuels.

Fuel and oxygen utilization can be calculated with Eqs. (19) and (20).

2.1.1.2. Porous media diffusion: Dusty-Gas Model

The porous media diffusion mechanism given in Table 2 provides the link between the electrochemistry taking place at the TPB and the gas chambers/channels system above the electrodes where the SOFC is fed with fuel and oxidizer gases. A schematic representation of the partial pressure distribution of the H_2 and H_2O fuel

Table 1
Governing equations for the main mass transport processes in the gas chambers (for 1D) and gas channels (for 2D and quasi-3D) (both denoted by subscript 'ch') and within the porous electrodes (el) for anode (an) and cathode (ca) side respectively. The domains for equations and variables as well as initial conditions (I.C.) and boundary conditions (B.C.).

Species conservation (s^{-1}) anode/cathode gas chambers (for 1D) [24]:

$$\frac{\partial Y_{ch,k}}{\partial t} = \frac{\dot{m}_{ch}^{in}}{\rho_{ch}V_{ch}}(Y_{ch,k}^{in} - Y_{ch,k}) + \frac{A_{cell}}{\rho_{ch}V_{ch}}\left(Y_{ch,k}\sum_{i=1}^{K_g}\dot{n}_i(0)\cdot MW_i - \dot{n}_k(0)\cdot MW_k\right) \qquad (14)$$

I.C.: $Y_{ch,k} = Y_{ch,k}^{in}$
for $k = 1$ to K_g, where K_g = number of gas phase species anode/cathode.

Species conservation ($kg\,m^{-3}\,s^{-1}$) anode/cathode gas channels (for 2D and quasi-3D) [25]:

$$\frac{\partial(\rho_{ch}Y_{ch,k})}{\partial t} = -\Delta(\rho_{ch}Y_{ch,k}u_{ch}) - \frac{W_{ch}\cdot MW_k}{A_{ch}}\bar{n}_k(0) \qquad \text{for } k = 1 \text{ to } K_g$$

algebraic sign changes to + for cathode in 2-D counter-flow mode $\qquad (15)$

$$\sum_k Y_{ch,k} = 1 \qquad (16)$$

I.C.: $Y_{ch,k} = Y_{ch,k}^{in}$, for $k = 1$ to $K_g - 1$

Domains:
  2D co-flow
  2D counter-flow
  Quasi-3D cross-flow

$x = (0: l_x]$ BFDM discretization (anode and cathode)
$x = (0: l_x]$ (BFDM, anode) and $x = [0: l_x)$ (FFDM, cathode)
$x = (0: l_x]$ and $y = [0: l_y]$ (BFDM, anode)
$x = [0: l_x]$ and $y = (0: l_y]$ (BFDM, cathode)

B.C.:
  2D co-flow
  2D counter-flow

  Quasi-3D cross-flow

For $k = 1$ to $K_g - 1$
Anode/cathode: $\quad Y_{ch,k}(0) = Y_{ch,k}^{in} \qquad u_{ch}(0) = u_{ch}^{in}$
Anode: $\quad Y_{ch,k}(0) = Y_{ch,k}^{in} \qquad u_{ch}(0) = u_{ch}^{in}$
Cathode: $\quad Y_{ch,k}(l_x) = Y_{ch,k}^{in} \qquad u_{ch}(l_x) = u_{ch}^{in}$
Anode: $\quad Y_{ch,k}(0,y) = Y_{ch,k}^{in} \qquad u_{ch}(0,y) = u_{ch}^{in}$
Cathode: $\quad Y_{ch,k}(x,0) = Y_{ch,k}^{in} \qquad u_{ch}(x,0) = u_{ch}^{in}$

Porous media transport anode/cathode ($mol\,cm^{-3}\,s^{-1}$) [25]:

$$\varepsilon\frac{\partial c_{el,k}}{\partial t} = -\frac{\partial \dot{n}_k}{\partial z} + a_{Ni}\dot{s}_k \qquad (17)$$

I.C.: $c_{el,k} = c_{ch,k}$

$$\sum_k X_{el,k} = 1 \qquad (18)$$

$\dot{s}_k = 0$ for $H_2/H_2O/N_2$ anode atmospheres and for cathode
for $k = 1$ to K_g

Domains: $z_{el} = (0: d_{el})$, $x = [0: l_x]$ (for 2D), $y = [0: l_y]$ (for quasi-3D)

B.C.: for anode/cathode
  $X_{el,k}(0) = X_{ch,k}$ (for $k = 1$ to $K_g - 1$)
  $P_{el,tot}(0) = P_{op}$
  $\dot{n}_k(d_{el}) = \nu_k \cdot \dot{r}_{TPB}$ (for $k = 1$ to K_g) where ν_k is the stoichiometric coefficient for the electrochemical
    reaction, i.e. +1 for H_2, −1 for H_2O and +0.5 for O_2 and 0 for others

$$U_f = \frac{I_{tot}\cdot V_m^0}{2F\cdot \dot{N}_{an}^{in}(X_{H_2}^{in} + X_{CO}^{in} + 4X_{CH_4}^{in})}, \quad \text{fuel utilization }(-) \qquad (19)$$

$$U_o = \frac{I_{tot}\cdot V_m^0}{4F\cdot \dot{N}_{ca}^{in}\cdot X_{O_2}^{in}}, \quad \text{oxygen utilization }(-) \qquad (20)$$

gas within the anode and the O_2 and N_2 oxidizer gas within the cathode is presented in Fig. 2.

The Dusty-Gas Model (DGM), developed by Mason and Malinauskas [21], is given by Eq. (21) which evaluates the species molar fluxes $\dot{n}_k$ for the porous media transport equations (Eq. (17)). The DGM is nowadays employed in most detailed SOFC models [2] and a comparison by Suwanwarangkul et al. [22] between different diffusion models found the DGM most applicable for SOFC modeling.

The binary diffusion coefficients given by Eq. (22) are evaluated according to Fuller et al. [26,27] which was found out to be the most accurate method for SOFC conditions by Todd and Young [28]. For the Knudsen diffusion coefficients, Eq. (24) was taken from Mills [29] and depends on the pore diameter and Knudsen diffusion that can get significant at pore diameters below 1 μm. All diffusion coefficients are corrected in Eq. (17) by the porosity and tortuosity to

account for the free gas pathways in the pores. According to Haberman and Young [30], the tortuosity has a quadratic influence on the effective diffusion coefficients which was later on confirmed and applied by DeCaluwe et al. [31].

2.1.2. Heterogeneous reaction mechanism for methane and syngas (HCR)

A multi-step heterogeneous reaction mechanism consisting of 42 irreversible elementary reactions ($I_{all} = 42$) as reported in [33,4] was employed to evaluate the source and sink terms of the methane/syngas mass transport through the porous electrodes. This mechanism, validated for Ni-YSZ cermets in SOFC applications for temperatures between 220 and 1700 °C, implicitly accounts for the water-gas-shift (WGS), methane reforming

Table 2
Equations and parameters for the Dusty-Gas diffusion model (DGM) and binary and Knudsen diffusion coefficients. All equations and variables are distributed within the closed domains $z_{an} = [0: d_{an}]$, $x = [0: l_x]$ (for 2D), $y = [0: l_y]$ (for quasi-3D). They account for anode and cathode and valid for $k,j = 1$ to K_g gas phase species.

Dusty-Gas Model equation (mol cm^{-4}) [21] without the viscous flux (pressure driven) term:
$$\frac{\partial c_{el,k}}{\partial z} = -\sum_{j \neq k}^{K_g} \frac{c_{el,j} \cdot \dot{n}_k - c_{el,k} \cdot \dot{n}_j}{c_{el,tot} \cdot (\varepsilon/\tau^2) \cdot D_{k,j}} - \frac{\dot{n}_k}{(\varepsilon/\tau^2) \cdot D_{KN,k}} \qquad (21)$$
Fuller et al. expression [27] for the binary diffusion coefficient (cm^2 s^{-1})
$$D_{k,j} = 0.00143 \cdot \frac{T^{1.75}}{P_{el,tot} \cdot MW_{k,j}^{0.5} \cdot (V_k^{1/3} + V_j^{1/3})} \qquad (22)$$
Fuller et al. diffusion volumes [28]:
H_2: 6.12, H_2O: 13.1, CH_4: 25.14, CO_2: 26.7, CO: 18.0, O_2: 16.3, N_2: 18.5
Binary molecular weight for binary diffusion coefficient evaluation according to Fuller et al:
$$MW_{k,j} = 2\left(\frac{1}{MW_k} + \frac{1}{MW_j}\right)^{-1} \qquad (23)$$
Knudsen diffusion coefficients determined from kinetic theory [29]:
$$D_{KN,k} = \frac{2 \cdot r_{pore}}{3} \cdot \left(\frac{8R_g T}{\pi \cdot MW_k}\right)^{0.5} \qquad (24)$$

and Boudouard reactions. The mechanism describes the adsorption ($I_{ad} = 6$) and desorption reactions of the 6 gas phase species ($K_{g,an} = 6$) H_2, CO, CH_4, CO_2, H_2O, O_2, and surface reactions of 13 surface species ($K_s = 13$) including the free Nickel catalyst sites, i.e. H_s, O_s, OH_s, HCO_s, C_s, CH_s, $CH_{2,s}$, $CH_{3,s}$, $CH_{4,s}$, CO_s, $CO_{2,s}$, H_2O_s and Ni_s. It is assumed that surface adsorption is limited to a mono atomic layer. In total, the system includes 19 chemical species ($K_{an} = 19 = K_{g,an} + K_s$) which take part in the 42 reactions. The reaction mechanism complies with the mass balances according to the law of mass-action kinetics with the formalism described in detail in [32] and given in brevity in Table 3. The 42 elementary reactions with the corresponding model parameters A_i (pre-exponential factor), β_i (temperature exponent), E_{ai} (activation energy), ε_i (surface site fraction-dependent activation energy) and γ_i can be found in [33,4].

2.1.3. Electrochemical model

2.1.3.1. Potentials and current

The potential step approach for cell potential evaluation is presented in detail in Section 1.1. For the models in this work, no distributed charge-transfer was applied, so that the charge-transfer and potential steps only occur lumped at the interfaces of electrodes (Ni-YSZ anode or LSM cathode) and electrolyte membrane as the assumed TPB.

The electrochemical model equations are given in Table 4. The total cell current Eq. (34) is the applied alternating current during EIS simulation from Eq. (45) and equals the sum of the locally distributed currents for the 2D and quasi-3D approach. The total current (or current density j given by Eq. (35)) originates from two different sources during transient operation. The Faradaic current I_F is directly proportional to the electrochemical reaction rate given by Faraday's law in Eq. (36). The electrical double-layer induced current depends on the double-layer capacitances C_{dl} and only exists during transient change of the half-cell potential steps as given by Eq. (37).

2.1.3.2. Butler–Volmer type activation overpotentials for charge-transfer reactions

The Butler–Volmer equation (40) relates the activation overpotential η_{act} to the Faradaic current density j_F. In this work, a modified Butler–Volmer type approach developed by Zhu et al. [34]

Table 3
Basic elements of HCR reforming kinetics from [32] according to law of mass-action. All equations and variables are distributed within the closed domains $z_{an} = [0: d_{an}]$, $x = [0: l_x]$ (for 2D), $y = [0: l_y]$ (for quasi-3D).

Species net molar production rate in (mol cm^{-2} s^{-1}), where ν_{ki} is the difference between stoichiometric coefficients of products and reactants of the kth species in the ith reaction:
$$\dot{s}_k = \sum_{i=1}^{I_{all}} \nu_{ki} \dot{r}_i, \quad \text{for } k = 1, \ldots, K_{an} \qquad (25)$$
Adsorption reaction rates (mol cm^{-2} s^{-1}) evaluated with sticking coefficient γ_i (between 0 and 1), where ν'_{ki} is the stoichiometric coefficient of reactant k in the ith reaction, where m_i is the sum of stoichiometric coefficients of surface species reactants in the ith reaction, and where Γ is the available surface site density (mol cm^{-2}):
$$\dot{r}_i = \frac{100 \cdot \gamma_i}{\Gamma^{m_i}} \sqrt{\frac{R_g T}{2\pi MW_i}} \cdot \prod_{k=1}^{K_{an}} c_{an,k}^{\nu'_{ki}}, \quad \text{for } i = 1, \ldots, I_{ad} \qquad (26)$$
Arrhenius type reaction rate (mol cm^{-2} s^{-1}) dependent on surface site fraction θ_{CO} (pre-exponential factor A, temperature coefficient β, activation energy E_a and coverage-dependent activation energy $e_{a,i}$ parameters from Maier et al. [33]), where ν'_{ki} is the stoichiometric coefficient of reactant k in the ith reaction:
$$\dot{r}_i = A_i T^{\beta_i} \exp\left(\frac{-E_{a,i}}{R_g T}\right) \exp\left(\frac{-e_{a,i}\theta_{CO}}{R_g T}\right) \cdot \prod_{k=1}^{K_{an}} c_{an,k}^{\nu'_{ki}}, \quad \text{for } i = I_{ad} + 1, \ldots, I_{all} \qquad (27)$$
Transient surface site fraction (s^{-1}) distribution:
$$\frac{\partial \theta_k}{\partial t} = \frac{\dot{s}_k}{\Gamma}, \quad \text{for } k = 1, \ldots, K_s - 1 \qquad (28)$$
I.C.: $\theta_k = 1E-7$
Conservation of surface site fractions:
$$\sum \theta_k = 1, \quad \text{for } k = 1, \ldots, K_s \qquad (29)$$
Surface species concentration (mol cm^{-2}):
$c_{an,k} = \theta_k \Gamma, \quad \text{for } k = 1, \ldots, K_s \qquad (30)$

Table 4
Equations for the electrochemical model [5]. All equations and variables are distributed within the closed domains $x = [0: l_x]$ (for 2D) and $y = [0: l_y]$ (for quasi-3D). They account for anode (el = an) and cathode (el = ca).

Cell voltage (in V) is not distributed because of equi-potential assumption:

$$E_{cell} = \Phi_{e,ca} - \Phi_{e,an}$$ (5)

B.C.: $\Phi_{e,ca} = 0$

Potential step between electron (e) and ion (i) conducting phases (in V):

$$\Delta \Phi_{el} = \Phi_{e,el} - \Phi_{i,el}$$ (6,7)

B.C.: $\Phi_{i,an} = \Phi_{i,ca} + R_{ohm} \cdot j$

Cathodic half-cell reduction potential (in V) for the half-cell reaction in Eq. (8):

$$\Delta \Phi_{eq,ca} = E^{\circ}_{O_2/O^{2-}} - \frac{RT}{2F} \ln \left(\frac{a_{O^{2-}}}{p_{O_2}^{0.5} \cdot a_{V_O^{\bullet\bullet}}} \right)$$ (9)

Anodic half-cell reduction potential (in V) for the half-cell reaction in Eq. (10):

$$\Delta \Phi_{eq,an} = E^{\circ}_{H_2O/H_2} - \frac{RT}{2F} \ln \left(\frac{p_{H_2} \cdot a_{O^{2-}}}{p_{H_2O} \cdot a_{V_O^{\bullet\bullet}}} \right)$$ (11)

Standard electromotive force (in V) at standard pressure depending only on temperature:

$$E^{\circ}_{el} = -\frac{\Delta G^{\circ}_{el}}{2F}$$ (31)

with $\Delta G^{\circ}_{el} = \Delta H_{el} - T \Delta S_{el}$ (32)

Nernst potential (in V) of the global electrochemical hydrogen oxidation reaction in Eq. (1):

$$E_{Nernst} = \Delta \Phi_{eq,ca} - \Delta \Phi_{eq,an}$$ (33)

Relationship between activation overpotential (in V) and potential steps:

$$\eta_{act,el} = \Delta \Phi_{el} - \Delta \Phi_{eq,el}$$ (12, 13)

Total cell current (in A) where I is the local current in distributed models (2D/quasi-3D):

$$I_{tot} = I \quad \text{for 1D}$$ (34)

$$I_{tot} = \sum I \text{ for 2D and quasi-3D}$$

Current density (in A cm^{-2}):

$$j = \frac{I}{A} = j_{F,el} + j_{dl,el}$$ (35)

for local current density 2D: $A = A_{cell}/(\text{\# of discretization intervals in } x + 1)$
for local current density quasi-3D: $A = A_{cell}/(\text{\# of discretization intervals } (x+1)(y+1))$

Faraday's law is the relation between electrochemical reaction rate and Faradaic current density (in mol cm^{-2} s^{-1}):

$$\dot{r}_{TPB} = \frac{j_F}{2F}$$ (36)

Double-layer current density (in A cm^{-2}) [7]:

$$j_{dl,el} = \pm C_{dl,el} \cdot \frac{\partial (\Delta \Phi_{el})}{\partial t}, \quad (- \text{ for cathode})$$ (37)

I.C.: $(\partial (\Delta \Phi_{el})/\partial t) = 0$

Ohmic resistance (in Ohm cm^2) through the dense electrolyte membrane:

$$R_{ohm} = \frac{d_{electrolyte}}{\sigma_i}$$ (38)

Electrolyte conductivity (in S cm^{-1}):

$$\sigma_i = \frac{\sigma_0}{T} \exp \left(-\frac{E_i}{R_g T} \right)$$ (39)

Table 5
Equations and parameters for the modified Butler–Volmer-type activation overpotential due to charge-transfer kinetics [34]. All equations and variables are distributed within the closed domains $x = [0: l_x]$ (for 2D) and $y = [0: l_y]$ (for quasi-3D). They account for anode (el = an) and cathode (el = ca).

Butler–Volmer equation (A cm^{-2}):

$$j_{F,el} = j_{0,el} \left[\exp \left(\frac{\alpha_{an,el} F \cdot \eta_{act,el}}{R_g T} \right) - \exp \left(-\frac{\alpha_{ca,el} F \cdot \eta_{act,el}}{R_g T} \right) \right]$$ (40)

with $\alpha_{an,el} = 1.5$ and $\alpha_{ca,el} = 0.5$

Anodic exchange current density (A cm^{-2}):

$$j_{0,an} = k_{H_2} \exp \left(-\frac{E_{H_2}}{R_g T} \right) \frac{(p_{H_2}(d_{an})/p_{H_2}^*)^{0.25} (p_{H_2O}(d_{an}))^{0.75}}{1 + (p_{H_2}(d_{an})/p_{H_2}^*)^{0.5}} \quad p \text{ in atm}$$ (41)

$$\text{with } p_{H_2}^* = \frac{A_{H_2} \Gamma^2 \sqrt{2\pi \cdot R_g \cdot T \cdot MW_{H_2}}}{10 \cdot \gamma_0} \exp \left(-\frac{E^{des}_{H_2}}{R_g T} \right) \quad \text{in atm}$$ (42)

with $A_{H_2} = 5.59E + 19$ cm^2 mol^{-1}s^{-1}, $\Gamma = 2.6E+9$ mol cm^{-2}, $E^{des}_{H_2} = 88,120$ J mol^{-1}, $\gamma_0 = 0.01$, $k_{H_2} = 207,000$ A cm^{-2}, $E_{H_2} = 87,800$ J mol^{-1}

Cathodic exchange current density (A cm^{-2}):

$$j_{0,ca} = -k_{O_2} \exp \left(-\frac{E_{O_2}}{R_g T} \right) \frac{(p_{O_2}(d_{ca})/p_{O_2}^*)^{0.25}}{1 + (p_{O_2}(d_{ca})/p_{O_2}^*)^{0.5}} \quad p \text{ in atm}$$ (43)

$$\text{with } p_{O_2}^* = A_{O_2} \exp \left(-\frac{E^{des}_{O_2}}{R_g T} \right) \quad \text{in atm}$$ (44)

with $A_{O_2} = 4.9E + 8$ atm, $E^{des}_{O_2} = 200,000$ J mol^{-1}, $k_{O_2} = 51,900$ A cm^{-2}, $E_{O_2} = 88,600$ J mol^{-1}

Table 6
Model equations for the simulation of the electrochemical impedance spectra (EIS).

$$I_{tot}(t) = I_{bias} - I_{gain} \cdot \sin(\omega \cdot t) \quad \text{sinusoidal alternating current} \tag{45}$$

$$\frac{\partial Time}{\partial t} = 1 \quad \text{I.C.: } Time = 0 \tag{46}$$

$$\omega = 2\pi \cdot f \quad \text{angular frequency in radians} \tag{47}$$

$$\nu = \frac{1}{f} \quad \text{period of the sinusoidal signal} \tag{48}$$

$$E_p \cdot \cos\varphi = 2f \cdot \int_0^\tau E_{cell}(t) \cdot \sin(\omega \cdot t)dt \quad \varphi \text{ in degrees} \tag{49.a}$$

$$\frac{\partial Z_1}{\partial t} = E_{cell}(t) \cdot \sin(\omega \cdot t) \quad \text{integrated by gPROMS}^{TM} \text{ for } t = 0 \text{ to } \nu \tag{49.b}$$

$$E_p \cdot \cos\varphi = 2f \cdot Z_1(\nu) \quad \text{evaluated by gPROMS}^{TM} \text{ at } t = \nu \tag{49.c}$$

$$E_p \cdot \sin\varphi = 2f \cdot \int_0^\tau E_{cell}(t) \cdot \cos(\omega \cdot t)dt \quad \varphi \text{ in degrees} \tag{50.a}$$

$$\frac{\partial Z_2}{\partial t} = E_{cell}(t) \cdot \cos(\omega \cdot t) \quad \text{integrated by gPROMS}^{TM} \text{ for } t = 0, \ldots, \nu \tag{50.b}$$

$$E_p \cdot \sin\varphi = 2f \cdot Z_2(\nu) \quad \text{evaluated by gPROMS}^{TM} \text{ at } t = \nu \tag{50.c}$$

$$Re(Z) = \frac{A_{cell} \cdot 10 \cdot E_p \cdot \cos\varphi}{I_{gain}} \quad (\text{Ohm cm}^2) \tag{51}$$

$$Im(Z) = -\frac{A_{cell} \cdot 10 \cdot E_p \cdot \sin\varphi}{I_{gain}} \quad (\text{Ohm cm}^2) \tag{52}$$

$$|Z| = \sqrt{Z_{real}^2 + Z_{im}^2} \quad (\text{Ohm cm}^2) \tag{53}$$

was employed, who derived expressions for the exchange current densities $j_{0,el}$ (Eqs. (41) and (43)) from elementary electrochemical kinetics for the assumed rate limiting reaction steps (Table 5).

2.1.3.3. EIS model

The model equations for the EIS simulation are given in Table 6. In Fig. 4, the simulation schedule of the computational procedure is presented: the steady-state current I_{bias} needs to be switched to the frequency- and time-dependent alternating sinusoidal current given by Eq. (45). It serves as the input signal for the EIS calculation. The gPROMS^{TM} dynamic solver implicitly integrates all transient equations (denoted by $ in gPROMS^{TM}) when a time schedule is given. No direct access to the time variable itself is allowed in the modeling section [35]. Since the equations for the EIS evaluation require explicitly the time variable, a dummy time variable, e.g. *Time*, needs to be introduced whose time derivative equals 1 as given by Eq. (46). This dummy time variable proceeds isochronic with the internal gPROMS^{TM} time variable.

The simultaneous evaluation of the two time integral Eqs. (49.a) and (50.a) determines the phase angle φ and the amplitude of the sinusoidal cell voltage E_p with which the real (Eq. (51)) and imaginary (Eq. (52)) parts of the impedance Z are calculated. These equations are obtained through trigonometric transformation of the general expression for the sinusoidal phase-shifted cell voltage output for a given sinusoidal current input [24]. In gPROMS^{TM}, this calculation is achieved by splitting up the problem into two steps. First, the time derivatives of Eqs. (49.a) and (50.a), given in Eqs. (49.b) and (50.b), are integrated over a full period ν and then at the end of the period (*Time* = ν) the results are used in Eqs. (49.c) and (50.c) to evaluate the impedance parameters. It has to be noted, that the system needs to be run for several periods (10 periods proved to be enough) to reach a periodic steady-state, before the impedance for a given frequency can be evaluated.

2.1.4. Computational procedure

Fig. 4 gives a schematic representation of the computational procedure for the EIS simulation. The model is fed with input values for the desired operational parameters, SOFC geometry, materials properties, etc. All governing and constitutive equations from Tables 1–6 are solved simultaneously with the inbuilt

gPROMS^{TM} solvers DASOLV (differential algebraic solver for the transient problem with absolute and relative tolerance 1E−12 and 1E−10) and SPARSE (non-linear algebraic solver for the spatially discretized problem with convergence tolerance of 1E−7). For numeric discretization of the spatially distributed equations, the finite difference method (FDM) was chosen in its different forms with a polynomial degree of 2. For the different domains, the following FDM methods and number of discretization intervals were chosen:

- z_{an}: centred finite difference method (CFDM), 10 intervals
- z_{ca}: CFDM, 4 intervals
- x: backward finite difference method (BFDM), 10 intervals for cathode channel in counter-flow configuration the forward finite difference method (FFDM) was chosen, 10 intervals
- y: backward finite difference method (BFDM), 10 intervals

A detailed simulation schedule has to be specified in order to produce a complete EIS from the solutions of a range of frequencies f for the alternating current Eq. (45) as the input signal.

3. Simulation results and discussion

3.1. V–j-curve and EIS of a base case simulation

The analysis of the inherent voltage losses (overpotentials) of an operating SOFC and the breaking down of these losses appearing in the electrochemical impedance spectrum (EIS) is carried out by means of a base case defined in Table 7. The simulations are run with the 1D model approximating button-cell experiments which are commonly used for new materials testing. The base case is defined for a typical laboratory scale anode supported cell (ASC) operating at a common SOFC temperature of 800 °C with humidified hydrogen. The simulations results presented here were evaluated with a fixed fuel and air inlet flow and thus varying fuel utilization U_f and oxidizer (oxygen/air) utilization U_o. Another option for the analysis is the fixation of U_f and U_o by adjusting the inlet fuel and air flow rates to the current density. This would fix the gas chamber bulk partial pressures for all points on the V–j-curve and thus the inlet boundary values for the porous electrode diffusion mechanism. Although the reversible Nernst potential related losses due to gas depletion in the gas chambers would be inhibited (preferable since these are purely thermodynamic losses and not related to cell material), this technique is not experimentally accessible since the required mass flow controllers cannot adjust the flow rates so quickly to the sinusoidal current perturbation (with frequencies up to 1 MHz). Section 3.5 shows also the EIS of methane and biomass derived syngas fuelled SOFCs. EIS results obtained with the 2D and quasi-3D models are comparatively shown in Section 3.6.

An overview of the base case performance is presented in Fig. 5 where its V–j-curve together with the curves for anode and cathode activation overpotentials from Eq. (40) and ohmic overpotential evaluated with Eq. (38) are given. In addition, the Nernst potential curves (Eq. (33)) evaluated for partial pressures at the reaction zones (triple phase boundary (TPB) at d_{an} and d_{ca}) and bulk gas chambers are shown. The former is the actual electrochemical potential for the global electrochemical hydrogen oxidation reaction while the latter represents the theoretically available potential, only affected by bulk gas depletion (due to changing U_f and U_o with the current density). Their difference accounts for the so-called concentration overpotential due to diffusion induced partial pressure gradients within the porous anode and cathode electrodes. This can further be split up into anodic and cathodic contributions by evaluating the respective half-cell potentials (Eqs. (9) and (11))
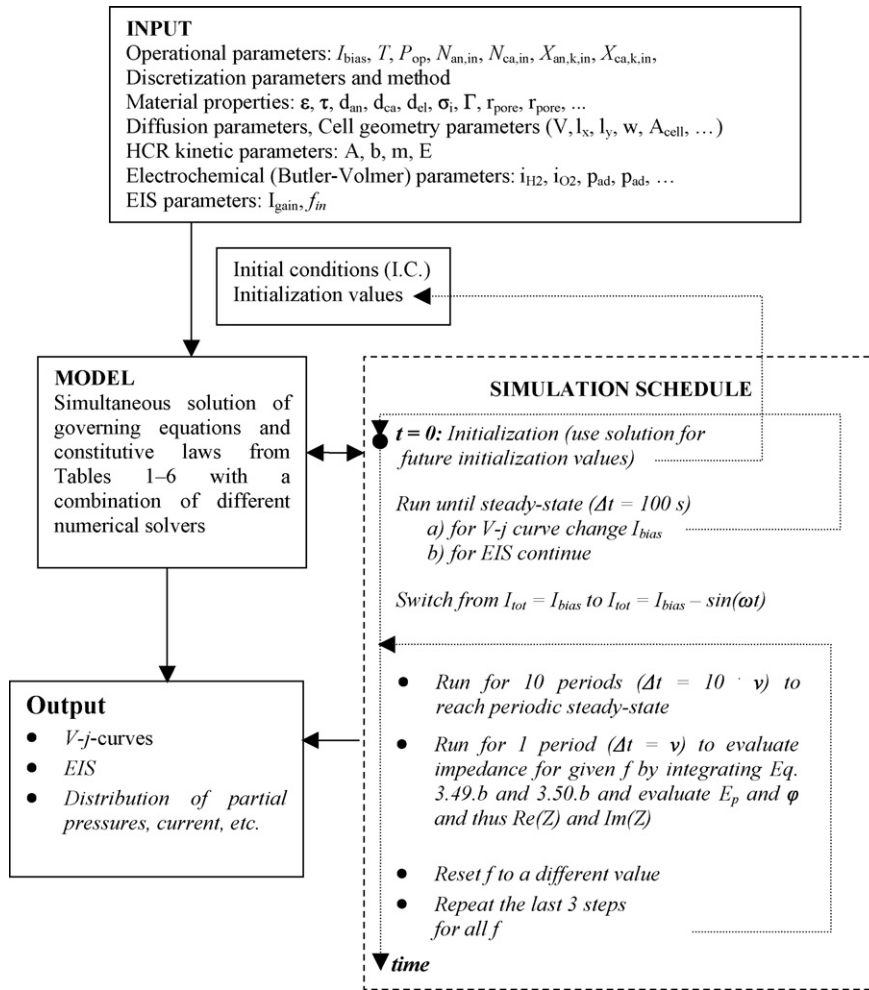
Fig. 4. Computational procedure.

for TPB and bulk gas partial pressures. Thus anode and cathode concentration overpotentials are plotted likewise in Fig. 5a and b shows the corresponding course of area-specific resistances vs. current density which can be evaluated by dividing the respective overpotentials by the current density: $R_i = \eta_i / j$. For selected current densities, simulated electrochemical impedance spectra (EIS)

obtained with the full loss model are presented in form of a Nyquist plot in Fig. 6.

The shape of the V–j-curve more or less follows the shape of the Nernst potential curve evaluated for partial pressures at the TPB. This typical shape of high non-linearity at low and high current densities and a rather linear part in between originates from the
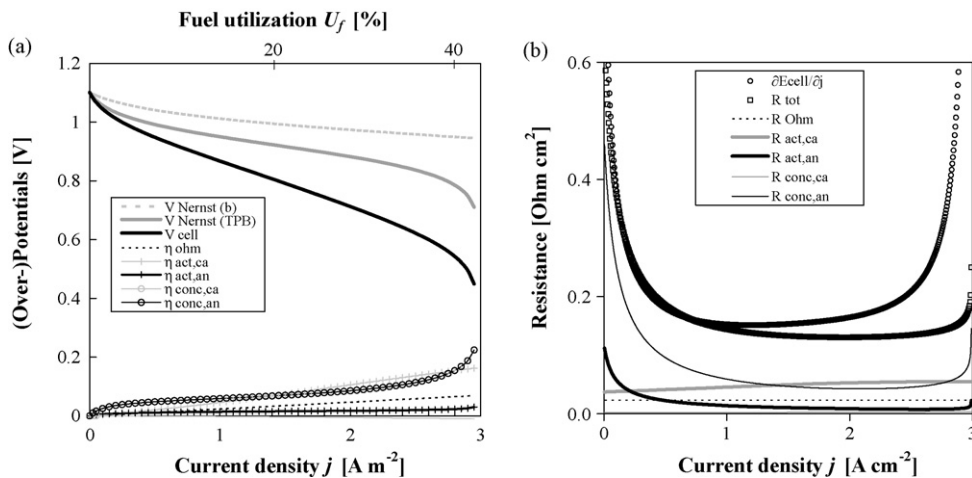

Fig. 5. Base case (BC) steady-state performance characteristics. (a) V–j-curve and the different Nernst- and overpotentials; (b) area-specific resistances of the different overpotentials, their sum the total resistance R_{tot} and the differential resistance $\partial E_{cell} / \partial j$ (slope of the V–j-curve).

Table 7
Model input values for a base case (BC) and the parametric analysis.

Parameter	Unit	Base case	Parametric analysis	Comment
Operational parameters				
P_{op}	bar	1.013	–	Cell pressure chamber/channels
T	°C	800	–	Cell Temperature
J_{bias}	A cm^{-2}	2.75	0–2.85	Bias current density for EIS
I_{gain}	A	0.1	–	Gain current amplitude for EIS
$N_{an,in}$	lt min^{-1}	0.5	0.5–2	Inlet anode volume flow
$X_{H_2,in}$	–	0.97	0.485	Inlet anode molar fraction hydrogen
$X_{H_2O,in}$	–	0.03	0.15	Inlet anode molar fraction steam
$X_{N_2,in}$	–	0	0.5	Inlet anode molar fraction nitrogen
$N_{ca,in}$	lt min^{-1}	2	–	Inlet cathode volume flow
$X_{O_2,in}$	–	0.2	–	Inlet cathode molar fraction oxygen
$X_{N_2,ca,in}$	–	0.8	–	Inlet cathode molar fraction nitrogen
Cell geometry				
l_{cell}	cm	3.16	–	Length/width of cell
l_x	cm	3.16	–	Cell length in x-direction (for 2D and quasi-3D)
l_y	cm	3.16	–	Cell length in y-direction (for quasi-3D)
$d_{electrolyte}$	µm	10	–	Electrolyte thickness
d_{an}	µm	500	0–500	Anode thickness
d_{ca}	µm	30	–	Cathode thickness
h_{an}, h_{ca}	mm	3	–	Height anode/cathode channels
w_{an}, w_{ca}	mm	2	–	Width anode/cathode under channel
A_{cell}	cm^2	10	–	Active cell area
V_{an}	m^3	1.517E−06	1.5E−5, 1.5E−7	Volume anode chamber
V_{ca}	m^3	1.517E−06	–	Volume cathode chamber
Materials properties				
ε	–	0.35	0.4, 0.45	Electrode porosity
τ	–	3.5	2, 3.1	Electrode tortuosity
r_{pore}	µm	0.5	0.75, 1	Electrode average pore radius
σ_0	S K^{-1} cm^{-1}	3.6E+5	–	Parameter for electrolyte conductivity
E_i	J mol^{-1}	80,000	–	Parameter for electrolyte conductivity
C_{dl}	F cm^{-2}	1E−4	1E−1, 1E−7	Anode double-layer capacitance
$j_{0,an}$	A cm^{-2}	Eq. 3.41	×0.1, ×10	Exchange current density

change of the partial pressure ratio p_{H_2}/p_{H_2O} with fuel utilization. The most dominant overpotentials for all current densities are the cathodic activation overpotential $\eta_{act,ca}$ and the anodic concentration overpotential $\eta_{conc,an}$ which can also be seen from the course of the resistances. While $\eta_{act,ca}$ increases rather linearly with the current density, $\eta_{conc,an}$ is highly non-linear (Nernst potential shape) and most dominant at low and high current densities. The sharp decline at high current density constitutes the limiting current density due to diffusion induced depletion of the hydrogen partial pressure p_{H_2} at the TPB. Additionally, close to OCV also the anodic activation overpotential is high but drops quickly with increasing current density j.

The ohmic overpotential has a medium effect (due to the thin electrolyte) and increases linearly due to its constant resistance R_{ohm} independent of j. The cathode concentration overpotential $\eta_{conc,ca}$ is rather negligible in this base case due to the high oxygen
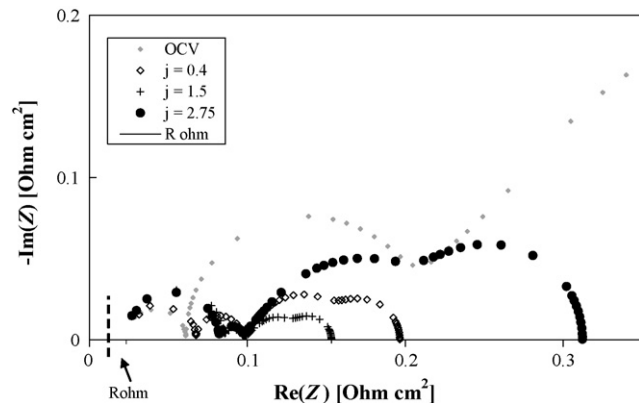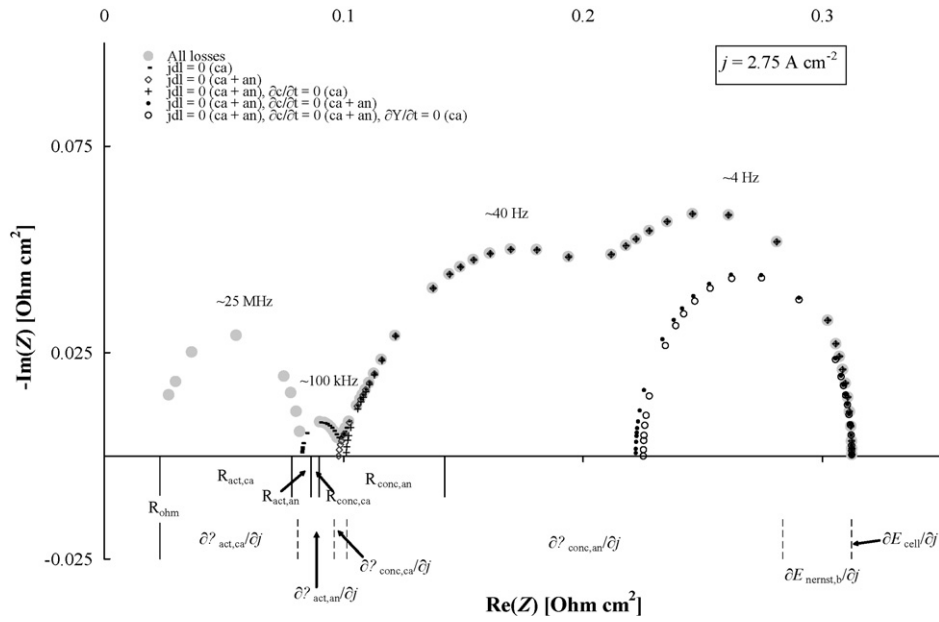
excess ratio (low U_o) and thin cathode porous electrode thickness (only small diffusion induced p_{O_2} gradient) employed.

By comparing the resistances from Fig. 5b with the EIS for different current densities given in Fig. 6, rough conclusions can already be drawn for the assignation of the different visible arcs. It is a common fact, that the ohmic resistance R_{ohm} has constant impedance independent of the frequency [11]. It manifests itself on the Re(Z) axis as the high-frequency intercept of the EIS.

The first visible high-frequency arc (left) describes a significant loss whose resistance is increasing with current density. Thus it must be related to the cathodic activation overpotential $\eta_{act,ca}$. The second high-frequency arc (to the right of the first arc) is large at OCV, then decreases with j; thus it can be related to the anodic activation overpotential $\eta_{act,an}$. Since the cathodic concentration overpotential $\eta_{conc,ca}$ is negligible small, the remaining anodic concentration overpotential $\eta_{conc,an}$ must be related to the two remaining middle and low frequency arcs. These follow the trend of $R_{conc,an}$ which is very high at low and high current densities and of similar magnitude in between. The origin of the two partially superimposed arcs will be investigated further below.

The preliminary findings of above are investigated in more detail in Fig. 7 by means of a step-by-step reduction of the influence of the different transport processes on the imaginary part of the EIS. This is carried out by setting the transient parts of the six transport processes (3 for cathode (ca) and 3 for anode (an)), i.e. double-layer current (j_{dl} in Eq. (37)), porous electrode diffusion ($\partial c/\partial t$ in Eq. (17)) and gas chamber species conservation ($\partial Y/\partial t$ in Eq. (14)) for anode and cathode, respectively, successively to zero and thus turning them into stationary equations. The losses of these mechanisms are still evaluated, but their capacitive nature is taken away, which means that the partial pressures are instantaneously adapting to the periodically varying current density.

The results confirm the above made preliminary analysis. The first high-frequency arc on the left (peak frequency $f_p \approx 25$ MHz) is

Fig. 6. Electrochemical impedance spectra (EIS) for different current densities chosen from the base case V–j-curve of Fig. 5.

Fig. 7. Base case EIS at $j = 2.75 \, A \, cm^{-2}$ (in the non-linear part of the V–j-curve close to current limiting behavior) with the full loss model and the subsequent reduction of the transient parts of the transport equations.

related to the cathodic activation overpotential because it disappears when setting the cathodic double-layer layer current to zero. As will be shown later on, the variation of activation overpotential specific parameters influence the magnitude of the double-layer related arc. Likewise, the second arc ($f_p \approx 100 \, kHz$) can be related to the anodic activation overpotential. As it was assumed, the cathode concentration overpotential turns out to be negligible while the anode concentration overpotential dominates and is related to the middle-frequency arc ($f_p \approx 40 \, Hz$), also called diffusion impedance. Additional information on the nature of the low frequency arc ($f_p \approx 4 \, Hz$) is revealed here. It remains as an effect of the anodic and cathodic gas chamber (perfectly stirred reactor) species conservation expressions where the cathodic contribution is negligible. Since it is related to the changing Nernst potential due to changing fuel and oxygen utilization, it can be called Nernst impedance. It is also called gas conversion impedance in literature [19,16,36].

The relationship between steady-state cell performance resulting from the Nernst potential reduced by different resistances (presented as V–j-curves) and the electrochemical impedance spectra is not straightforward. The Re(Z)-axis low frequency intercept constitutes the total impedance Z_{tot} which is equal to the slope of the V–j-curve $\partial E_{cell}/\partial j$ at the investigated current [19,10]. However, no clear relationship between calculated resistances given in Fig. 5b and the width of the impedance arcs of the different transport processes can be established. Fig. 7 additionally provides the calculated resistances R_i and differential resistances ($\partial \eta_i/\partial j$) which are cumulatively plotted at the Re(Z)-axis. Both of them do not collide with the impedance arcs intercepts.

The previous analysis revealed which anode and cathode related main losses can be seen in the EIS. For the sake of brevity, the further investigation of the three main loss mechanisms by means of a parametric analysis in the following sections will only be carried for the anodic system. The nature of the cathode related losses are equivalent to the anode and both can be regarded as two decoupled systems. Thus all cathodic transient terms are set to zero, in order to suppress their imaginary impedance components. The varied parameters for the analysis of the three main losses are included in Table 7.

Fig. 8 shows how the impedance arcs come about by presenting the dynamic periodic variation of important SOFC operation variables at four different frequencies f. The variables are plotted for two periods during the EIS simulation and are normalized with the respective value at the beginning of each period (given in Table 8). The origin of the impedance arcs are the phase-shifted cell potential E_{cell} (output signal) when applying a sinusoidal alternative current density j (input signal). The phase shift occurs due to capacitive behavior of the different subsystems, described by the transport equations, and produces imaginary impedance.

At high frequency (100 kHz), a double-layer induced current density $j_{dl,an}$ occurs which adds up together with the Faradaic current density $j_{F,an}$ to the total current density j. Both $j_{dl,an}$ and $j_{F,an}$ are phase shifted with respect to j and thus account for a phase-shifted cell potential E_{cell}. All other important variables (with a slight exception of $p_{H_2,TPB}$) are constant because they are not sensitive to the high frequency. Since $j_{F,an}$ is directly related to the activation overpotential, the emerging double-layer impedance arc at high frequencies due to electrical double-layer capacitance is also related to the activation overpotentials.

At medium frequency (100 Hz), all variables except the anodic gas chamber hydrogen partial pressure $p_{H_2,ch}$ show a periodic course. The double-layer induced current is almost zero and thus $j_{F,an}$ is in line with j. Here, the phase-shifted variable responsible for the phase-shifted E_{cell} is the hydrogen partial pressure at the TPB $p_{H_2,TPB}$. The intermediate frequency impedance arc thus can be attributed to concentration overpotentials due to diffusion induced losses through the porous anode electrode.

At low frequency (5 Hz), all variables show a periodic course. Here, the gas chamber hydrogen partial pressure $p_{H_2,ch}$ is phase

Table 8
Variable values at the beginning of each period during EIS simulation.

Variable	Unit	100 kHz	100 Hz	5 Hz	0.1 Hz
j	$A \, cm^{-2}$	2.75	2.75	2.75	2.75
E_{cell}	mV	560.08	559.76	559.60	560.13
$p_{H_2,b}$	bar	0.59481	0.59482	0.59414	0.59476
$p_{H_2,TPB}$	bar	0.0834	0.0828	0.0826	0.0834
$j_{F,an}$	$A \, cm^{-2}$	2.755	2.750	2.750	2.750
$j_{dl,an}$	$A \, cm^{-2}$	−4.96E−03	~0	~0	~0
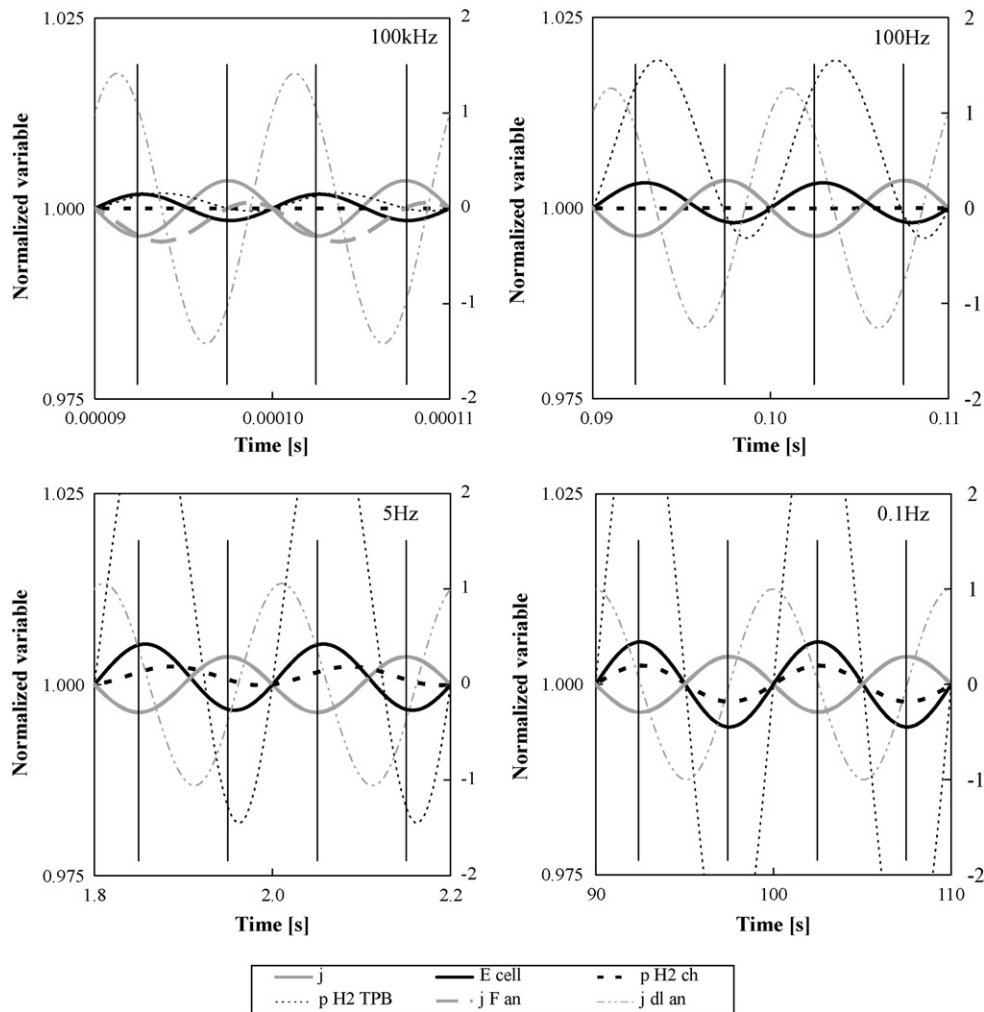
Fig. 8. Dynamic variation of some important variables for two periods during EIS simulation shown for four different frequencies f. The variable values are normalized with the respective value at the beginning of the period.

shifted in addition to $p_{H_2,TPB}$ and is responsible for the low frequency Nernst impedance arc.

At very low frequency (0.1 Hz), all variables are varying periodically in line with j and thus no phase shift exists.

3.2. Variation of anode gas chamber related parameters

This section describes how the variation of anode gas chamber related parameters affects the EIS, especially the low frequency Nernst impedance arc.

Fig. 9 shows the influence of changing anode gas chamber volume V_{an}. Decreasing the volume to 10% of the base case (BC) value shifts the Nernst impedance arc to higher frequencies merging with the diffusion impedance arc. The Nernst impedance is affected due to the changing fuel gas flow velocity when the gas chamber volume is varied. A ten times larger V_{an} results in an almost complete separation of diffusion and Nernst impedance arcs where the latter is shifted towards a ten times lower peak frequency. Two cases are presented additionally where only the Nernst impedance arc occurs by setting all other transient terms to zero. The variation of V_{an} however does not affect the total impedance Z_{tot} and thus also not SOFC performance. A numerical relationship for the variation of this arc is given by Primdahl and Mogensen [16].

The Nernst impedance arc does not exist when the fuel utilization is kept constant (by setting the gas chamber partial pressures to the outlet values of the steady-state results). When the transient part of the gas chamber transport equation (Eq. (14)) is set to zero, the gas chamber mass fractions follow instantaneously the current and diffusion and Nernst impedance arcs merge. This extreme is approached when V_{an} is set to very small values.

Fig. 10 shows the influence of changing the anode gas inlet flow $N_{an,in}$. An increase of the inlet fuel flow results in a shift of the Nernst impedance arc towards higher frequencies until it merges with the diffusion impedance arc at very high flows (due to the high gas flow velocities). Higher fuel flows at constant current densities imply smaller fuel utilization and thus higher hydrogen partial pressures. This results in decreased diffusion losses and thus also smaller total impedance Z_{tot}.

Fig. 11 shows the influence of changing fuel composition. When the base case gas composition is diluted with N_2 by 50%, the diffusion induced losses increase significantly due to the smaller hydrogen inlet partial pressure and the additional large molecule compound N_2. When the diluted flow is doubled, the same amount of hydrogen is entering the SOFC (allowing the same fuel utilization) as for the base case, however diffusion induced losses are still more than twice as large.

3.3. Variation of diffusion mechanism related parameters

The gas diffusion induced impedance arc has a typical shape. The semi-circle exhibits an almost linear slope (~45° angle) at the
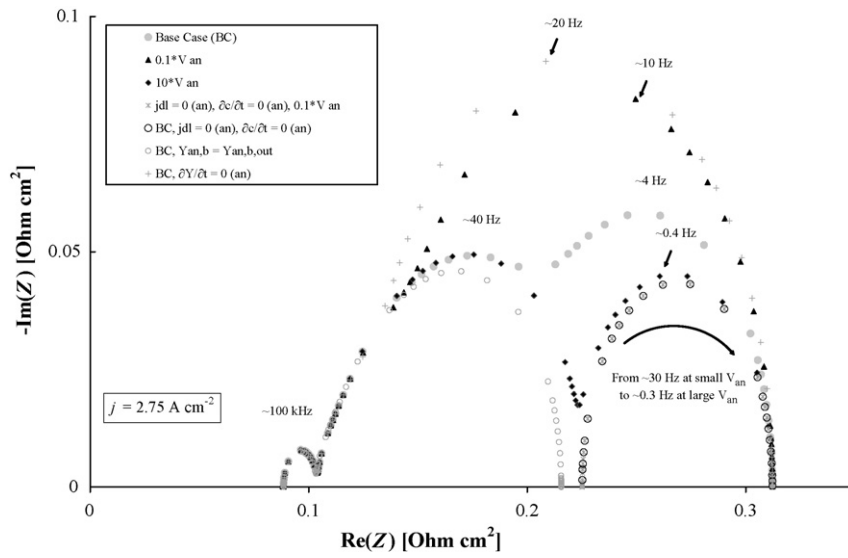
Fig. 9. EIS of base case and for the variation of anode gas chamber volume V_{an}. Additional cases with only the Nernst impedance arc and without the Nernst impedance arc are shown.
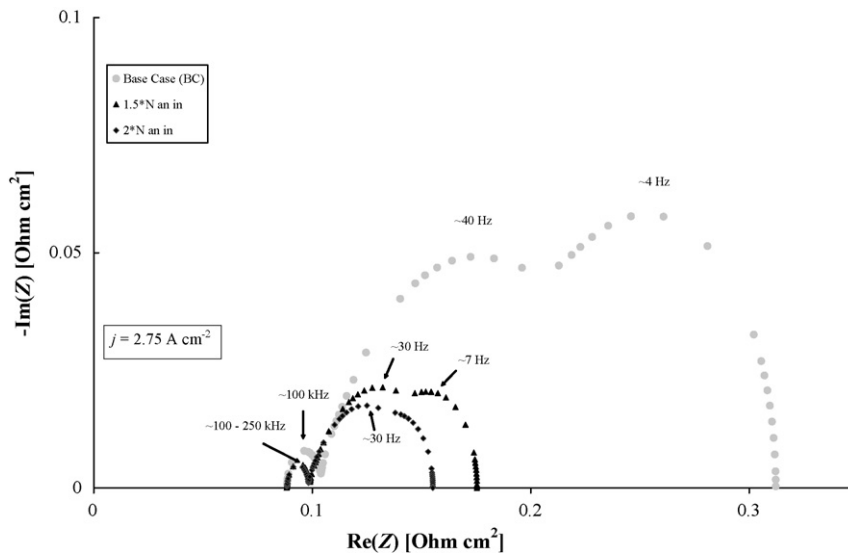

Fig. 10. EIS of base case and for the variation of anode gas inlet flow $N_{an,in}$.
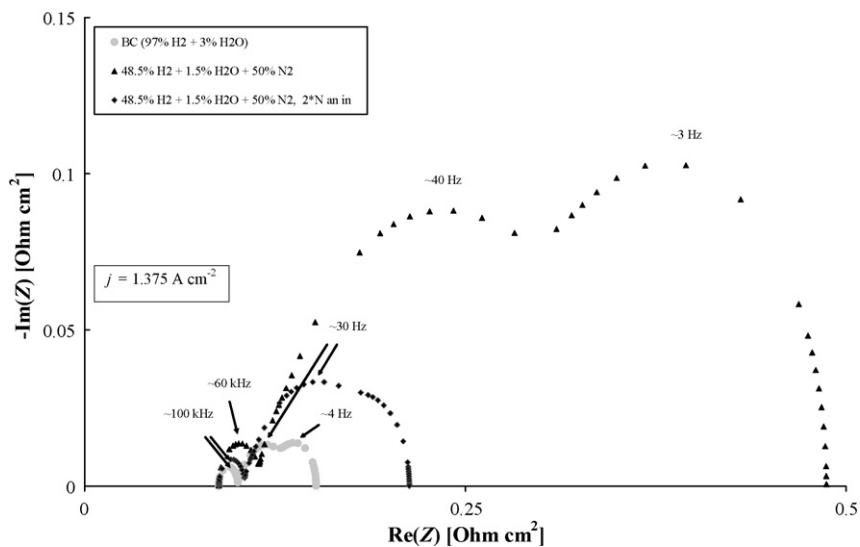

Fig. 11. EIS of base case and for different anode gas mixture with additional nitrogen.
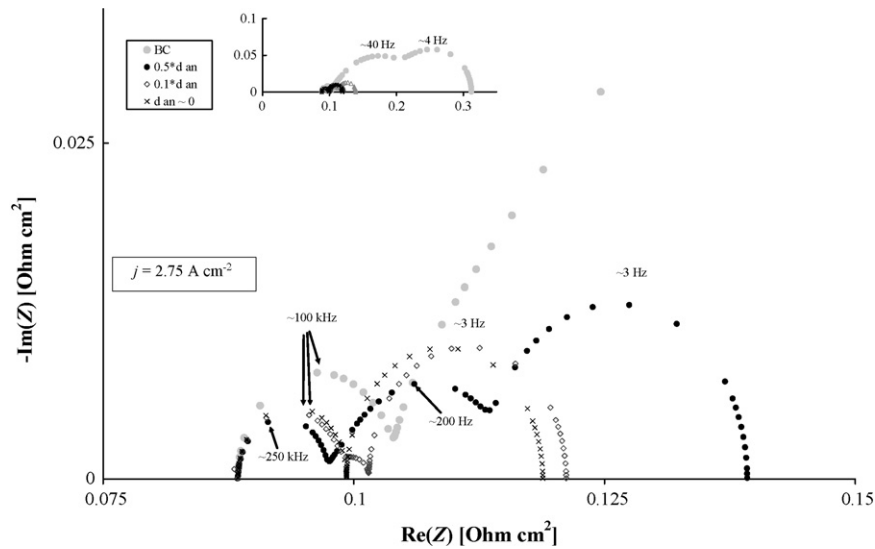
Fig. 12. EIS of base case and for the variation of anode thickness d_{an}.

higher frequency part of the arc (left side). This phenomenon is called Warburg impedance [10].

Fig. 12 shows the influence of changing the porous anode electrode thickness d_{an}. A decrease of d_{an} results in a shift of the diffusion impedance arc towards higher frequencies (due to smaller mass capacitance) and a reduction in the arc size due to smaller diffusion resistance. An infinitely thin anode ($\sim 0\,\mu m$) does not exhibit the middle-frequency diffusion impedance arc anymore. Only the double-layer and Nernst impedance arcs remain.

Figs. 13–15 show the effect of varying characteristic material properties which affect the gas diffusion through the porous electrodes. Higher porosity ε, larger average pore diameter r_{pore} and smaller tortuosity τ (non-linear pathway which the gas needs to pass through) all result in a decrease of the size of the diffusion impedance arc due to decreased diffusion losses.

3.4. Variation of double-layer capacitance and activation overpotential related parameters

Concerning the choice of base case values for the two double-layer capacitances (anodic and cathodic), $C_{dl,an}$ was chosen in an

order of magnitude given in literature [24] and $C_{dl,ca}$ was arbitrarily set 1000 times smaller in order to see separated arcs in the impedance spectra. Fig. 16 shows the variation of the two double-layer capacitances and their effect on the EIS. Setting both parameters to equals values results in only one double-layer impedance arc due to superimposition of the two arcs. The double-layer impedance arcs shift proportionally with the capacitances increase towards lower frequencies and start overlapping also the impedance arcs of the other transport processes. Theoretically speaking, if realistic double-layer capacitance values would be higher than, e.g. 1E−3 F cm^{-2}, it would get difficult to differentiate between the different losses since all arcs would be superimposed by the double-layer impedance arc. For small double-layer capacitances, it is possible to relate the arcs to the activation overpotentials. The high-frequency arcs due to cathodic or anodic double-layer capacitances might not appear in real EIS measurements since they can occur at frequencies higher than 100 kHz which is the typical highest frequency measured. A high-frequency shoulder observed in experiments is sometimes interpreted as an erroneous artifact, but in fact could possibly be the beginning part of an additional double-layer impedance arc.
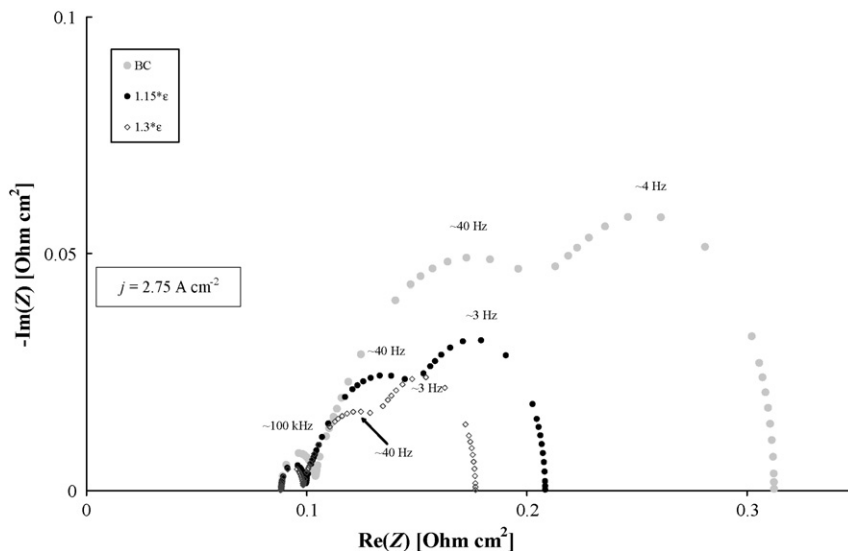

Fig. 13. EIS of base case and for the variation of anode porosity ε.
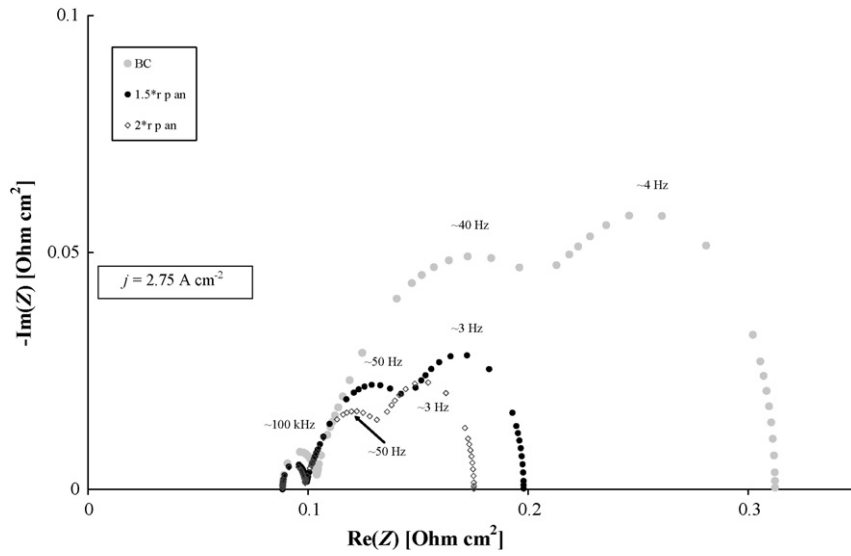
Fig. 14. EIS of base case and for the variation of anode average pore radius r_{pore}.
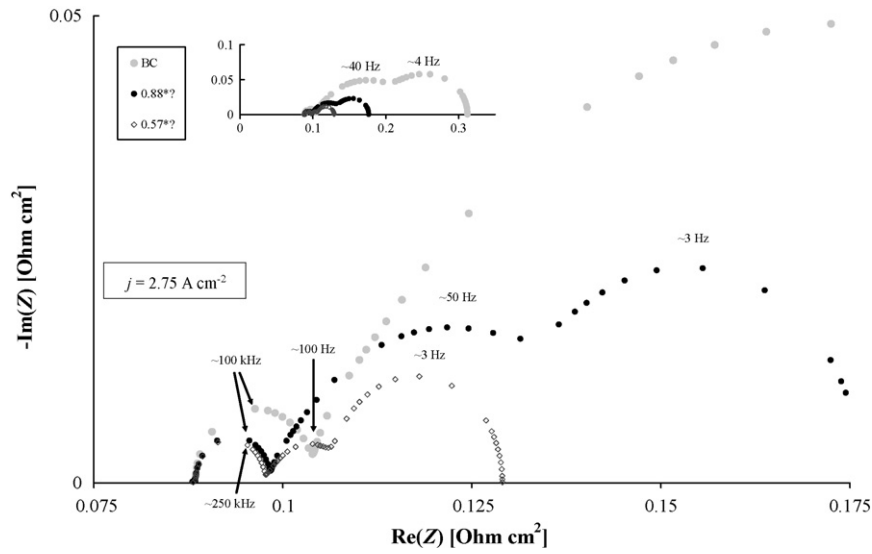

Fig. 15. EIS of base case and for the variation of anode tortuosity τ_{an}.
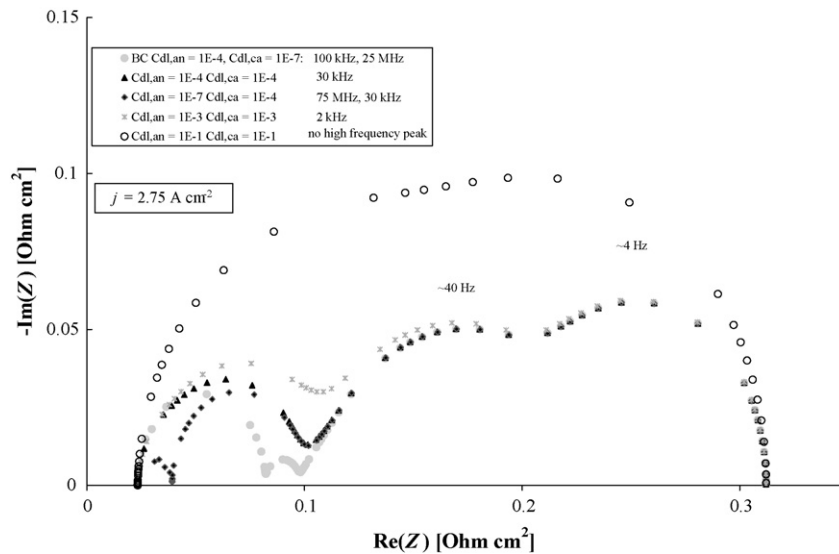

Fig. 16. EIS of base case and for the variation of anodic and cathodic double-layer capacitances $C_{dl,an}$ and $C_{dl,ca}$. The high-frequency arcs peaks are given next to the legend where the first value is due to the anodic and the second due to the cathodic double-layer contribution.
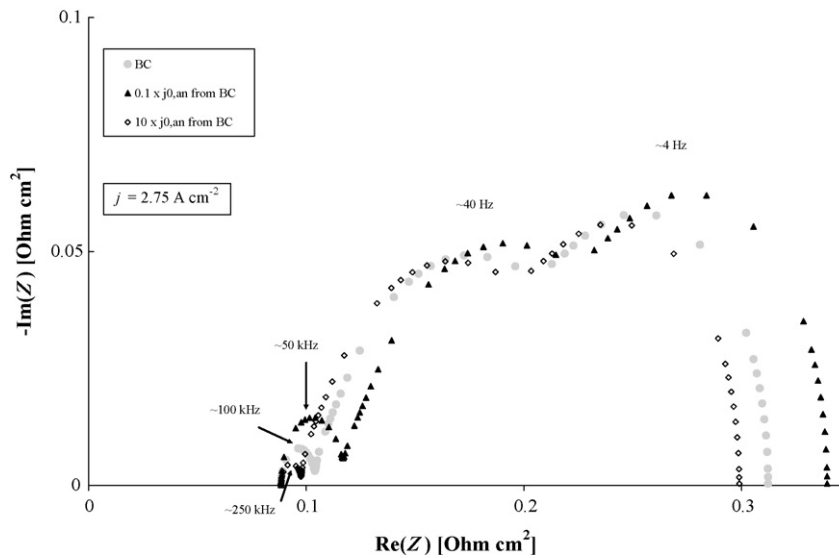
Fig. 17. EIS of base case and for the variation of anodic exchange current density $j_{0,an}$.

Fig. 17 shows the influence of changing anodic exchange current density $j_{0,an}$ which describes the kinetics of the anodic charge-transfer reaction. Decreasing $j_{0,an}$ to 10% of the base case (BC) value shifts the double-layer impedance arc to lower frequencies and increases its resistance. Accordingly a ten times larger $j_{0,an}$ results in a shift of the double-layer impedance arc towards higher frequencies with decreased resistance. This shows, that double-layer impedance arcs are related to the activation overpotentials.

3.5. Syngas 1D EIS

This subsection presents the influence of methane and biomass derived producer gas fuels on the EIS in comparison with the base case (BC) humidified hydrogen fuel. The anode inlet flow $N_{an,in}$ for each fuel was adjusted to match the hydrogen inlet mass flow of the base case when considering complete methane reforming and CO shift. The steam diluted methane is fed to the SOFC with a steam-to-carbon ratio of 2.5 which is a typical composition to avoid carbon deposition problems [37]. The methane reforming and water-gas-shift reactions are evaluated with the detailed heterogeneous catalytic reaction mechanism (HCR) given in Table 3. An important parameter determining the catalytic reaction rates is the specific nickel catalyst surface a_{Ni} which allows higher production rates when the value is high.

For the simulations presented in Fig. 18, the anode thickness d_{an} was varied in order to study the relation of the HCR with the porous electrode diffusion to which it is linked via the source and sink term of the porous media transport Eq. (17). A decrease of the anode thickness by a factor of 10 decreases the middle-frequency diffusion impedance related arc and also the total impedance Z_{tot}. Although less catalytic active sites for reforming are available in a thinner anode, the decreased diffusion resistance dominates and explains the increase in SOFC performance. A further decrease of the anode thickness by a factor of 10 results in a large total impedance Z_{tot}. Although the diffusion impedance is close to zero, a large medium to low frequency impedance arc occurs which must be related to the slow reforming rates due to the small amount of catalytic active sites resulting in less available hydrogen for the electrochemical reaction.
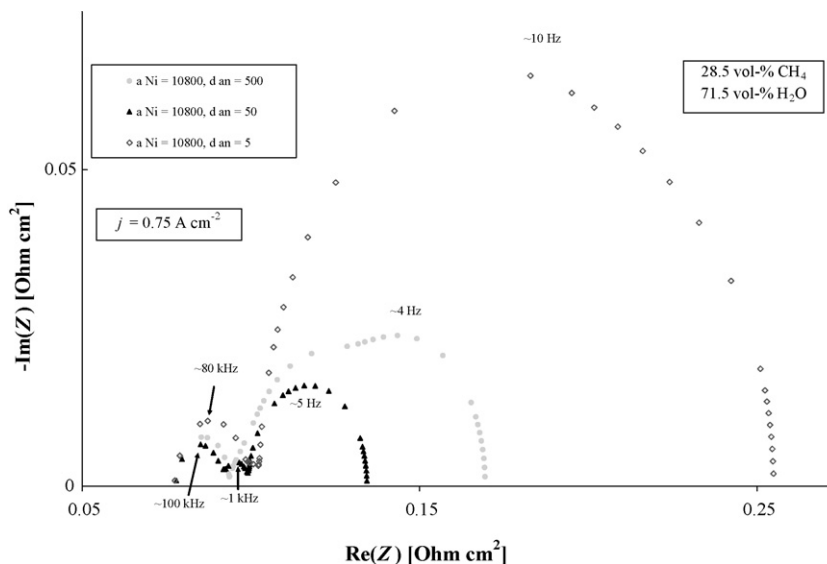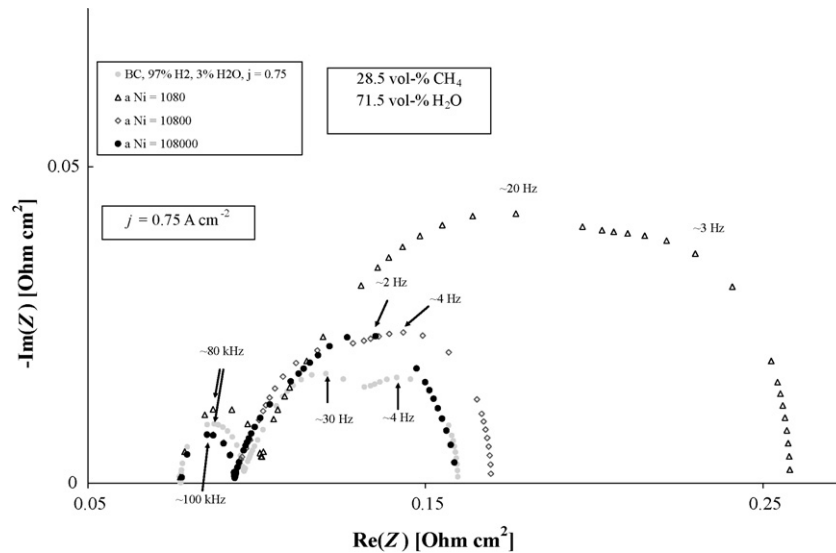

Fig. 18. EIS of a methane fuelled SOFC where the anode thickness d_{an} is varied.

Fig. 19. EIS of a methane fuelled SOFC with a steam-to-carbon ratio (H_2O:CH_4) = 2.5 where the specific nickel surface a_{Ni} is varied. Also the hydrogen fuelled base case is given for comparison.

Fig. 19 shows the influence of varying the specific nickel catalyst surface a_{Ni} allowing for slower or faster catalytic reactions producing hydrogen. The higher the amount of active catalytic sites, the faster is the production of hydrogen and the total impedance Z_{tot} of the hydrogen fuel base case EIS is approached. Smaller values of a_{Ni} result in increased total impedance due to less available hydrogen. In this case, the middle-frequency arc related to the porous media transport (diffusion) increases significantly where the catalytic reactions must play a major role.

Finally a comparison of the EIS obtained for three different hydrocarbon containing fuels at same operating conditions is given in Fig. 20. These are (1) the steam diluted methane from above, (2) a biomass producer gas from the air-blown two-stage fixed bed downdraft biomass gasifier "Viking" [38] with high nitrogen content and (c) a biomass producer gas from the circulating fluidized bed gasifier at Güssing [39] with high steam content due

to steam used as gasification agent. The inlet gas compositions for those cases are given in Table 9.

It can be seen that the producer gas fuel from the Viking gasifier shows by far the highest total impedance due to a large diffusion impedance arc. The cause of this is the high content of the large molecules nitrogen, carbon monoxide and carbon dioxide which increase the diffusion resistance within the porous anode.

Table 9
Biomass syngas fuel compositions.

[mol%]	Viking gasifier [38]	Güssing gasifier [39]
X_{H_2}	23.1	25.8
X_{CO}	12.93	15.0
X_{CH_4}	1.57	6.0
X_{CO_2}	14.08	12.0
X_{H_2O}	13.0	40.0
X_{N_2}	35.3	1.2
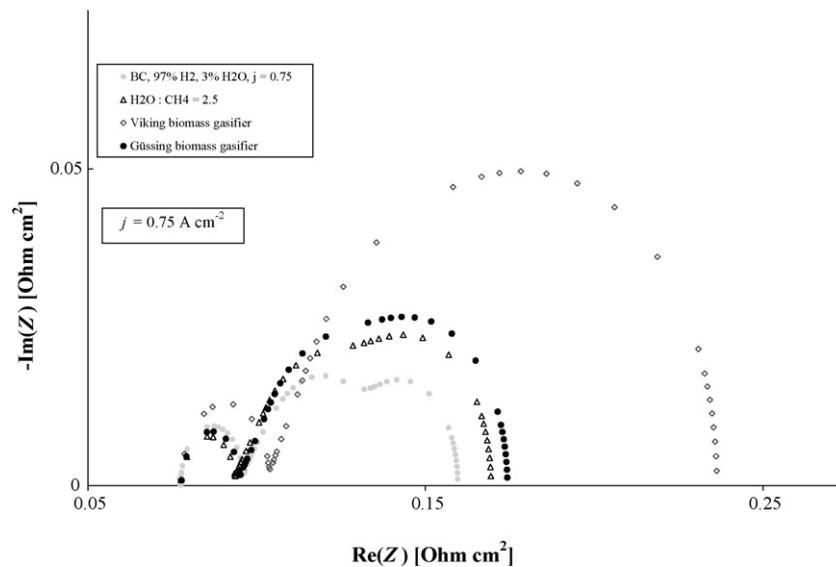
Fig. 20. EIS of three cases with different kinds of fuels. H_2O:CH_4 = 2.5, biomass derived producer gas from the Viking gasifier [39–3.41] and biomass derived producer gas from the Güssing gasifier [40–3.42]. Also the hydrogen fuelled base case is given for comparison.
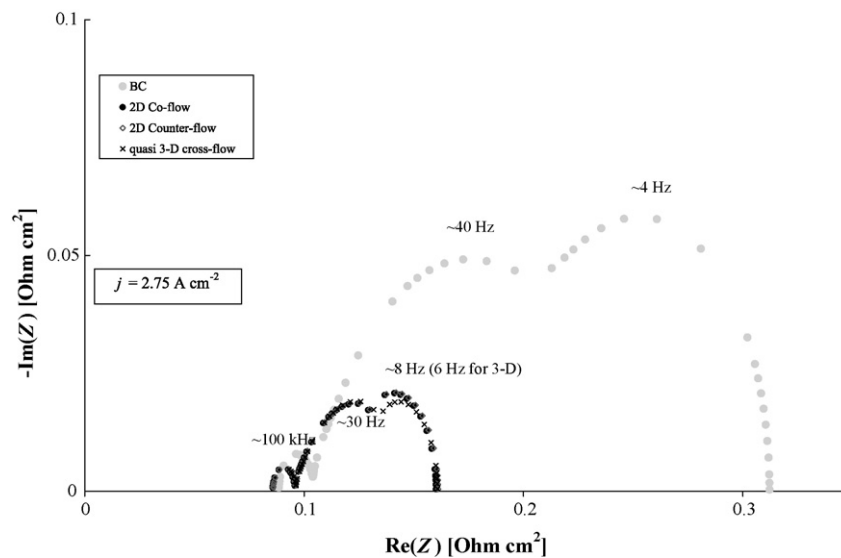
Fig. 21. EIS of the base case produced with the 1D, 2D (co- and counter-flow) and quasi-3D models.

The steam diluted producer gas fuel from the Güssing gasifier shows decreased diffusion impedance and approaches the total impedance of the steam diluted methane fuel. The total impedance is higher for all hydrocarbon fuels compared to the operation on humidified hydrogen due to increased diffusion impedance and smaller hydrogen partial pressures reducing the Nernst potential.

3.6. EIS of 1D, 2D and quasi-3D models

Fig. 21 shows the influence of different planar SOFC flow configurations on simulated EIS. A button-cell approximation (1D) with a homogeneous gas composition above the porous electrodes, co-flow and counter-flow channel configurations (2D) where gas channel partial pressures are distributed along the length of the channels in x-direction and a cross-flow channel configuration (quasi-3D) where anode partial pressures are distributed along the x-direction and cathode partial pressures along the y-direction are compared. The 2D and quasi-3D cases are comparable and show much smaller total impedance than obtained for the 1D case.

4. Conclusions

This paper presents a successful implementation of a dynamic planar SOFC model on the commercially available modeling and simulations platform gPROMS^{TM}. The special feature of the model is its capability to simulate electrochemical impedance spectroscopy (EIS), which is a common experimental SOFC performance analysis and diagnostic tool. All the necessary equations, parameters, boundary and initial conditions, that allow easy reproduction of the model, are presented.

The model based on physico-chemical governing equations is flexible to simulate different fuels ranging from hydrogen over methane to syngas, e.g. biomass derived producer gas. Different planar SOFC geometries can be investigated: button cells which are experimentally used to evaluate new materials (approximated by a 1D model only discretized in the gas diffusion direction through the porous electrodes), co- and counter-flow (2D model) and cross-flow (quasi-3D) gas channel configurations which describe real sized cells.

The model was applied in a detailed parametric analysis of the SOFC inherent losses (overpotentials) in an attempt to deconvolute the impedance spectrum of an SOFC. Each of the considered main transport processes can be attributed to an impedance arc.

However, general overlapping of several arcs makes it difficult to assess the underlying loss mechanisms in EIS measurements. The model facilitates the interpretation of EIS. The mass transport above the electrodes produces a low frequency impedance arc called Nernst impedance. Mass transport through the porous electrodes (due to diffusion) causes the concentration impedance arc in middle-frequency range of the EIS. In case of hydrocarbon fuels, the reforming reactions additionally affect this arc. The double-layer charge transport induces a current at the triple phase boundary and only exists during dynamic SOFC operation. It is related to the activation overpotentials and is responsible for the high-frequency arc. The observations account for the anodic as well as the cathodic systems.

The variation of the transport processes capacitances results in a shift of the process specific peak frequencies (characteristic relaxation time) but does not affect the resistances. Increasing the capacitance (e.g. mass or volume in the gas chambers and channels above the electrodes) makes the process relaxation slower and thus results in a shift of the impedance arc towards lower frequencies. The transport processes resistances are related to the width of the impedance arcs but no direct relationship could be obtained. The total impedance coincides with the slope of the V–j-curves (differential resistance) at a specific current.

Its special capability of simulating electrochemical impedance spectroscopy makes the model an important tool for analyzing SOFC fundamentals as well as for design, materials and operational parameters optimization and SOFC failure diagnosis. This allows for a reduction in the amount of costly experiments.

Acknowledgements

References

[1] R. Bove, S. Ubertini, Modeling Solid Oxide Fuel Cells: Methods, Procedures and Techniques (Fuel Cells and Hydrogen Energy), first ed., Springer Science + Business Media B.V., 2008.

[2] S. Kakaç, A. Pramuanjaroenkij, XiangYang Zhou, Int. J. Hydrogen Energy 32 (2007) 761–786.

[3] M.A. Khaleel, J. Robert Selman, Cell, stack and system modeling, in: S.C. Singhal, K. Kendall (Eds.), High Temperature Solid Oxide Fuel Cells: Fundamentals, Design and Applications, Elsevier, Oxford, 2003, pp. 291–331.

[4] V.M. Janardhanan, O. Deutschmann, J. Power Sources 162 (2006) 1192–1202.
[5] W.G. Bessler, Electrochemistry and Transport in Solid Oxide Fuel Cells, Universität Heidelberg, Habilitationsschrift, 2007.
[6] R.J. Kee, H. Zhu, A.M. Sukeshini, G.S. Jackson, Sci. Technol. 180 (2008) 1207–1244.
[7] W.G. Bessler, S. Gewies, M. Vogler, Electrochim. Acta 53 (2007) 1782–1800.
[8] B.A. Boukamp, Solid State Ionics 169 (2004) 65–73.
[9] Q. Huang, R. Hui, B. Wang, J. Zhan, Electrochim. Acta 52 (2007) 8144–8164.
[10] J. Ross Macdonald, Impedance Spectroscopy: Theory, Experiment and Applications, second ed., Wiley, 2005.
[11] Electrochemical Impedance Spectroscopy Primer, Gamry Instruments, 2005, Available at http://www.gamry.com.
[12] Daria Vladikova, The technique of the differential impedance analysis. Part 1. Basics of the impedance spectroscopy, in: Proceedings of the International Workshop "Advanced Techniques for Energy Sources Investigation and Testing", Sofia, Bulgaria, September 4–9, 2004.
[13] M. Cimenti, A.C. Co, V.I. Birss, J.M. Hill, Fuel Cells 7 (2007) 364–376.
[14] M. Cimenti, V.I. Birss, J.M. Hill, Fuel Cells 7 (2007) 377–391.
[15] P. Hofmann, K.D. Panopoulos, L.E. Fryda, E. Kakaras, Energy, doi:10.1016/j.energy.2008.09.015.
[16] S. Primdahl, M. Mogensen, J. Electrochem. Soc. 145 (1998) 2431–2438.
[17] S. Primdahl, M. Mogensen, J. Electrochem. Soc. 146 (1999) 2827–2833.
[18] W.G. Bessler, J. Electrochem. Soc. 153 (2006) A1492–A1504.
[19] K. Takano, S. Nagata, K. Nozaki, A. Monma, T. Kato, Y. Kaga, A. Negishi, K. Kato, T. Inagaki, H. Yoshida, K. Hosoi, K. Hoshino, T. Akbay, J. Akikusa, J. Power Sources 132 (2004) 42–51.
[20] W.G. Bessler, S. Gewies, J. Electrochem. Soc. 154 (2007) B548–B559.
[21] E.A. Mason, A.P. Malinauskas, Gas Transport in Porous Media: the Dusty-Gas Model, American Elsevier, New York, 1983.
[22] R. Suwanwarangkul, E. Croiset, M.W. Fowler, P.L. Douglas, E. Entchev, M.A. Douglas, J. Power Sources 122 (2003) 9–18.
[23] H. Zhu, R.J. Kee, J. Electrochem. Soc. 155 (2008) B715–B729.
[24] H. Zhu, R.J. Kee, J. Electrochem. Soc. 153 (2006) A1765–A1772.

[25] R. Bove, S. Ubertini, J. Power Sources 159 (2006) 543–559.
[26] E.N. Fuller, P.D. Schettler, J.C. Giddings, Ind. Eng. Chem. 58 (1966) 19–27.
[27] B.E. Poling, J.M. Prausnitz, J.P. O'Connell, The Properties of Liquids & Gases, fifth ed., McGraw-Hill, New York, 2000.
[28] B. Todd, J.B. Young, J. Power Sources 110 (2002) 186–200.
[29] A.F. Mills, Heat and Mass Transfer, Irwin, Chicago, 1995.
[30] B.A. Haberman, J.B. Young, J. Fuel Cell Sci. Technol. 3 (2006) 312–321.
[31] S.C. DeCaluwe, H. Zhu, R.J. Kee, G.S. Jackson, J. Electrochem. Soc. 155 (2008) B538–B546.
[32] R. Kee, R. Coltrin, P. Glarborg, Chemically Reacting Flow: Theory and Practice, Wiley and Sons, New York, 2003.
[33] L. Maier, V.M. Janardhanan, B. Schaedel, O. Deutschmann, Surface Reactions: Methane Reforming Kinetics Within A Ni–YSZ SOFC Anode Support, Version 1.2, ITCP, University of Karlsruhe, Germany, 2006, March. Available at: http://www.detchem.com/mechanisms.
[34] H. Zhu, R.J. Kee, V.M. Janardhanan, O. Deutschmann, D.G. Goodwin, J. Electrochem. Soc. 152 (2005) A2427–A2440.
[35] gPROMS™ Documentation, Release 3.0.4, Process Systems Enterprise Limited, Bridge Studios, London, 2007, November 2007.
[36] A. Momma, Y. Kaga, K. Takano, K. Nozaki, A. Negishi, K. Kato, T. Kato, T. Inagaki, H. Yoshida, K. Hosoi, K. Hoshino, T. Akbay, J. Akikusa, M. Yamada, N. Chitos, Solid State Ionics 174 (2004) 87–95.
[37] R.M. Ormerod, in: S.C. Singhal, K. Kendall (Eds.), High-temperature Solid Oxide Fuel Cells: Fundamentals, Design and Applications, Elsevier Science, Oxford, 2003, pp. 333–361.
[38] P. Hofmann, A. Schweiger, L. Fryda, K.D. Panopoulos, U. Hohenwarter, J.D. Bentzen, J.P. Ouweltjes, J. Ahrenfeldt, U. Henriksen, E. Kakaras, J. Power Sources 173 (2007) 357–366.
[39] R. Rauch, H. Hofbauer, Zweibett-Wirbelschichtvergasung in Güssing (A) mit 2MWel/4,5MWth; Konzept, Betriebserfahrungen und Wirtschaftlichkeit, in: Proceedings of 7 Holzenergiesymposion, ETH Zürich, Switzerland, October 18, 2002, 2002, See also: http://members.aon.at/biomasse/zuerich.pdf (in German).